Research Square

Preprints are preliminary reports that have not undergone peer review.
They should not be considered conclusive, used to inform clinical practice,
or referenced by the media as validated information.

Multimodal interrogation establishes the AAA+ ATPase RUVBL1 as a prognostic driver and tractable dependency in malignant pleural mesothelioma

Serif Senturk

serif.senturk@ibg.edu.tr

Izmir International Biomedicine and Genome Institute https://orcid.org/0000-0003-3963-2294

Medine Zeynep Gungor

Izmir International Biomedicine and Genome Institute

Ece Cakiroglu

Izmir International Biomedicine and Genome Institute

Sude Eris

Dokuz Eylul University https://orcid.org/0000-0002-2310-8829

Minenur Ozturk

Izmir International Biomedicine and Genome Institute

Zeynep Bayramoglu

Medical School

Buse Akdemir

Izmir International Biomedicine and Genome Institute

Gokcen Omeroglu Simsek

Medical School

Volkan Karacam

Medical School

Eyup Sabri Ucan

Medical School

Article

Keywords: Malignant pleural mesothelioma, RUVBL1, therapeutic target, CB-6644

Posted Date: August 14th, 2026

DOI: https://doi.org/10.21203/rs.3.rs-9380290/v1

License: This work is licensed under a Creative Commons Attribution 4.0 International License.
Read Full License

Additional Declarations: There is no conflict of interest

Multimodal interrogation establishes the AAA+ ATPase RUVBL1 as a prognostic driver and tractable dependency in malignant pleural mesothelioma

Medine Zeynep Gungor [1,2], Ece Cakiroglu [1,2], Sude Eris [1,2,*], Minenur Ozturk [1,2,*], Zeynep Bayramoglu [3], Buse Akdemir [1,2], Gokcen Omeroglu Simsek [4], Volkan Karacam [5], Eyup Sabri Ucan [4], Serif Senturk [1,2,#]

1 Izmir Biomedicine and Genome Center, Izmir, Türkiye

2 Dokuz Eylul University, Izmir International Biomedicine and Genome Institute, Izmir, Türkiye

3 Dokuz Eylul University, Faculty of Medicine, Department of Medical Pathology, Izmir, Türkiye

4 Dokuz Eylul University, Faculty of Medicine, Department of Chest Diseases, Izmir, Türkiye

5 Dokuz Eylul University, Faculty of Medicine, Department of Thoracic Surgery, Izmir, Türkiye

* These authors contributed equally to this work.

Correspondence

Prof. Dr. Serif Senturk

Research Group Leader

Functional Cancer Genomics Group

Izmir Biomedicine and Genome Center

Dokuz Eylul University

Health Campus Mithatpasa St. No: 58/5

35340 Balcova, Izmir / Turkey

Phone 1: 90 (232) 412 65 14

Phone 2: 90 (232) 299 41 61

E-mail: serif.senturk@ibg.edu.tr

Abstract

Malignant pleural mesothelioma (MPM) is an inexorably lethal malignancy, yet its therapeutic landscape remains largely devoid of actionable drivers. Here, by leveraging a stringent prioritization framework on genome-scale CRISPR dependency maps integrated with orthogonal molecular interrogation, we identify the AAA+ ATPase RUVBL1, an obligate component of the RUVBL1/2 complex, as a non-redundant and pharmacologically tractable vulnerability in MPM. This liability reflects a network-level addiction to RUVBL1/2-containing multiprotein assemblies, operating as survival hubs where subunit integrity appears indispensable. Genetic depletion of RUVBL1 induces profound cytostasis and cytotoxicity, compromising tumor cell fitness and clonogenic expansion in adherent monolayers and multicellular spheroids. Mechanistically, RUVBL1 loss triggers canonical replication stress with destabilization of the PIKK family kinases ATM and ATR. This leads to γH2AX accumulation, induction of p21, and activation of apoptotic signaling, enforcing checkpoint engagement and subsequent cell death. In contrast, ectopic RUVBL1 expression amplifies proliferative kinetics and potentiates aggressive traits, including epithelial-to-mesenchymal transition (EMT), invasion, and anchorage-independent growth. Correlative transcriptomics consensually links RUVBL1 to core oncogenic programs governing DNA damage repair, cell fitness, and EMT plasticity. Remarkably, pharmacologic inhibition of the RUVBL1/2 complex phenocopies the hallmarks of genetic perturbation. Clinically, tissue microarray profiling demonstrates significantly elevated RUVBL1 in mesothelioma, while multi-cohort analyses position it as a disease-specific marker and negative prognostic indicator. Critically, patient-derived, treatment-naïve *ex vivo* MPM cultures retain tumor-intrinsic RUVBL1 expression and exhibit strong sensitivity to ATPase inhibition, providing preclinical validation in patient-proximal models. Together, our findings establish RUVBL1 as a bona fide driver of MPM pathobiology and nominate the RUVBL1/2 complex as a rational target for therapeutic exploitation.

Keywords: Malignant pleural mesothelioma, RUVBL1, therapeutic target, CB-6644

Introduction

Malignant pleural mesothelioma (MPM) is a rare tumor of the pleural mesothelial lining that accounts for the majority of mesothelioma cases and remains a paradigm of therapeutic recalcitrance among solid tumors [1]. Driven principally by occupational and environmental asbestos exposure, MPM follows a dismal clinical trajectory with median overall survival stagnating below 12 months despite intensive multimodal regimens [2]. The genomic landscape of MPM is defined by a relatively modest tumor mutational burden and a paucity of activating oncogenic lesions. Instead, it is dominated by copy-number alterations, structural rearrangements, and complex chromatin derangements that converge on recurrent, near-universal inactivation of key tumor suppressor genes, including the deubiquitinase *BAP1*, the Hippo pathway regulator *NF2*, and the cell cycle guardians *CDKN2A* and *TP53* [3,4]. This pervasive loss of checkpoint control, together with widespread epigenetic dysregulation, fuels profound genomic and replicative instability and imposes chronic stress on macromolecular integrity.

The precision oncology armamentarium, historically centered on kinase inhibitors, has so far delivered limited benefit in MPM [5–7]. While immune checkpoint blockade has improved survival over historical controls, therapeutic outcomes remain modest and highly heterogeneous. Critically, efforts to potentiate clinical responses by combining immunotherapy with targeted signaling inhibitors have largely failed to overcome the disease's intrinsic resistance [8,9]. This clinical landscape accentuates a conceptual pivot from interrogation of conventional drivers toward a focus on exposing non-canonical addictions that are indispensable for tumor survival. Experience from other malignancies acknowledges that enzymes involved in DNA repair, chromatin remodeling, and metabolic adaptation can serve as high-value targets. The clinical success of PARP inhibitors in homologous recombination-deficient cancers [10], and the targeting of epigenetic modulators like EZH2 or metabolic regulators like mutant IDH1/2 [11,12], demonstrates that catalytic enzymes can be effectively and safely exploited as therapeutic nodes. In MPM, systematic identification of kinase and non-kinase enzymatic hubs that buffer DNA repair, sustain chromatin architecture, and transcriptional homeostasis represents a critical and largely untapped frontier.

RUVBL1 (RuvB-like 1; Pontin) is an evolutionarily conserved AAA+ ATPase with homology to the bacterial RuvB helicase. Together with its paralog RUVBL2 (RuvB-like 2; Reptin), RUVLB1 assembles into an obligate heterohexamer that functions not merely as a helicase, but

as a central co-chaperone scaffold for large macromolecular machines. Within the R2TP complex (or PAQosome), in association with HSP90, RPAP3 and PIH1D1, RUVBL1/2 are essential for the maturation of numerous multiprotein assemblies, including RNA polymerase II, small nucleolar RNPs, and PI3K-like kinase (PIKK) signaling complexes such as ATM/ATR and mTORC1 [13]. Beyond the R2TP axis, RUVBL1/2 are core components of ATP-dependent chromatin remodelers (e.g. INO80, TIP60, SWR1/SRCAP), integrating energy-driven remodeling into transcriptional regulation and homologous recombination repair. The hexamer can engage multiple adaptor proteins and alternative co-chaperone subunits, generating distinct PAQosome variants with tailored client repertoires and enable a single RUVBL1/2 hub to nucleate a broad interaction network [14–17]. Consistent with this centrality, RUVBL1 has been implicated in diverse oncogenic programs, amplifying the activity of proto-oncogenes (e.g. MYC and β-catenin) and driving proliferative machineries, while promoting transcriptional reprogramming associated with epithelial-to-mesenchymal transition (EMT) [18–21]. High RUVBL1 expression correlates with aggressive, treatment-refractory phenotypes and poor prognosis in a variety of solid tumors [22]. Despite this, the functional role and therapeutic relevance of RUVBL1 in the genomically unstable landscape of MPM remain unknown.

Here, by integrating post hoc reanalysis of genome-scale CRISPR genetic screens with mechanistic interrogation, we identify RUVBL1 as a druggable dependency in MPM. Using two- (2D) and three-dimensional (3D) culture systems and patient-derived preclinical models, we show that genetic depletion or pharmacologic inhibition of RUVBL1 induces catastrophic replication stress, leading to G2/M or S-phase arrest and apoptosis. RUVBL1 expression stratifies clinical outcomes, distinguishing malignant tissues from benign pleura and correlating with aggressive disease progression. Importantly, our findings suggest that MPM cells depend not only on RUVBL1, but on the broader set of RUVBL1/2-containing complexes. Together, our study unveils RUVBL1 as a previously unrecognized Achilles' heel in MPM, providing a rationale for therapeutically targeting this enzymatic hub in an otherwise intractable cancer.

Material and Methods

Cell culture

Human malignant pleural mesothelioma (MPM) cell lines H2052 (NCI-H2052; CRL-5915) and H2452 (NCI-H2452; CRL-5946) were obtained from the American Type Culture Collection (ATCC; Manassas, VA) and maintained in RPMI-1640 medium (21875034, Gibco)

supplemented with 10% fetal bovine serum (FBS; 10500064, Gibco) and 1% penicillin–streptomycin (15140122, Gibco). HEK293T cells were cultured in high glucose Dulbecco's Modified Eagle Medium (DMEM; 41965039, Gibco) supplemented with 10% FBS and 1% penicillin-streptomycin. All cultures were maintained at 37°C in a humidified incubator with 5% CO2, and were routinely screened for mycoplasma contamination using a PCR-based detection kit (G238, ABM).

Collection and processing of tumor specimens and culturing of primary cells

Patients deemed eligible for surgical resection by the Department of Chest Diseases or Thoracic Surgery, Dokuz Eylul University, were prospectively enrolled in the study. Ethical approval was granted by Dokuz Eylul University Ethics Committee for Non-Interventional Studies (approval number: 2024/02-19), and written consent was secured from both participants. Histopathologic diagnosis and subtype classification were confirmed via hematoxylin and eosin (H&E) staining and immunohistochemistry. Fresh tumor tissues were transported in a sterile transfer medium [Advanced DMEM/F12 (12634010, Gibco) containing 10 mM HEPES (15630080, Gibco), 1% Penicillin-Streptomycin (15140122, Gibco), 1X Glutamax (35050061, Gibco), 250 ng/mL Amphotericin B (15290026, Gibco), 15% Fetal Bovine Serum (10500064, Gibco) and 100 µg/mL Primocin (ant-pm-5, Invivogen)]. Tumors were minced using sterile surgical blades and subjected to enzymatic digestion in a cocktail containing Advanced DMEM/F12 (12634010, Gibco), 10 mM HEPES (15630080, Gibco), 1% Penicillin-Streptomycin (15140122, Gibco), 1X Glutamax (35050061, Gibco), 5 mg/mL Collagenase type II (17101015, Gibco), 100 µg/mL DNase I (D5025, Sigma), 10 µM Y-27632 (HY-10583, MedChemExpress), 1 mg/mL Dispase II (D4693, Sigma) and 2.5 µg/mL Amphotericin B (15290026, Gibco). Digestion was carried out at 37°C for 1 h on an orbital shaker (120 rpm) to obtain single-cell suspensions. Cell suspensions were passed through 100 µm sterile cell strainers (43-50100-51, pluriSelect), centrifugated at 200 × g for 10 minutes at 4 °C, and subjected to red blood cells were lysis (A1049201, Gibco) with gentle pipetting at room temperature for 5 min. After a second centrifugation step, cells were washed twice with ice-cold AdDMEMF12+++ [Advanced DMEM/F12 (12634010, Gibco) containing 10 mM HEPES (15630080, Gibco), 1% Penicillin-Streptomycin (15140122, Gibco), 1X Glutamax (35050061, Gibco)] to remove residual lysis buffer and plated in tissue culture-treated dishes under standard conditions (37°C, 5% CO2, and 90% humidity). Media was replaced every three days, and cultures were passaged at 1:2-1:3 ratios using Trypsin solution. Early-passage MPM tumor primary cultures (MPM-TPCs) were cryopreserved, and expanded cultures were used for

downstream experiments. Under these conditions, cultures could be stably maintained for at least 13 weeks.

Vector construction

Guide RNAs (gRNAs) targeting human RUVBL1 were selected from the Brunello genome-wide CRISPR library (Addgene #73178). A non-targeting control gRNA against *Renilla* luciferase (gRen) was used as a negative control. Oligonucleotides (Macrogen, South Korea) (Supplementary Table 1) were cloned into either lentiCRISPR v2 (Addgene #52961) or pECPV vectors (pEFS-Cas9-P2A-Venus), following previously described protocols [23]. For ectopic expression experiments, the RUVBL1 coding sequence was excised from the pCDNA-3xFLAG-Pontin plasmid (Addgene #51635) using BamHI (R3136S, NEB) and XbaI (R0145S, NEB), and ligated into the predigested pLV-EF1α-IRES-Puro backbone (Addgene #85132). gRNA-resistant RUVBL1 constructs were generated by overlapping PCR and cloned into pLV-EF1α-IRES-Puro. All lentiviral constructs were propagated in Stbl3 chemically competent *E. coli* (Invitrogen), screened by colony PCR, and verified by Sanger sequencing. Plasmid DNA was isolated using the EZ-10 Spin Column Plasmid DNA Miniprep Kit (BS614, BioBasic). A complete list of oligonucleotide sequences used is provided in Supplementary Table 2.

Lentiviral packaging and cell transduction

LLentivirus production was performed in HEK293T cells using standard third-generation packaging protocols. Cells were co-transfected with the target lentiviral vector, psPAX2 (Addgene #12260) and pMD2.G (Addgene #12259) helper vectors using polyethylenimine (PEI; 23966, Polysciences), as previously described [24]. Virus-containing supernatants were harvested 48 h post-transfection, filtered through 0.45 μm SFCA filters (431220, Corning), and immediately used for transduction. Target cells were seeded at ~50-60% confluency and infected with viral supernatants in the presence of 8 μg/mL polybrene (H9268, Sigma Aldrich) for 48 h. Infected populations were either selected with puromycin (ant-pr-1, Invivogen) or sorted based on Venus fluorescence using FACSAria III (BD Biosciences).

Cell proliferation assays

For competitive cell proliferation experiments, H2052 and H2452 cells were transduced with pECPV vector encoding gRNAs targeting *Renilla* luciferase or human RUVBL1. Transduced (Venus-positive) cells were quantified by flow cytometry using (LSRFortessa, BD), as previously described [24]. For bromodeoxyuridine (BrdU) incorporation assays, cells were seeded on coverslips in 24-well plates and pulse-labeled with 30 μM BrdU for 12 h. Cells were

fixed with 70% cold ethanol on ice for 10 min, followed by incubation with 2N HCl for 20 min to facilitate DNA denaturation. The coverslips were incubated with anti-BrdU antibody (1/1000; 5292, Cell Signaling Technology) for 2 h, followed by secondary staining with donkey anti-mouse Alexa Fluor 488 (1/500; ab150105, Abcam) for 1 h. Nuclei were counterstained with DAPI (1322MG005, Neofroxx). Images were acquired using fluorescence microscopes (Olympus BX61 or IX71). BrdU incorporation (%) was quantified as the ratio of BrdU-positive nuclei to total DAPI-positive nuclei across random fields. To evaluate pharmacologic inhibition, cells were treated with CB-6644 at three concentrations (0.5×IC50, IC50, and 2×IC50) for 72 h prior to BrdU labeling.

MTT assay

Cells were seeded in 96-well plates, and viability was assessed at 48, 96, 144, and 192 h post-seeding. At each time point, 20 µL of MTT solution (0.5 mg/mL final; 1334GR001, Neofroxx) was added per well and incubated for 4 h at 37°C. After removing the medium, 100 µL DMSO (LC-5071.2, Neofroxx) was added to solubilize the formazan crystals. Absorbance was measured at 570 nm (reference: 720 nm) using a Multiskan GO microplate reader (Thermo Fisher Scientific). To determine the IC50 of CB-6644, cells were seeded 1,500 cells/well in 96-well plates. After 24 h, the medium was replaced with increasing concentrations of CB-6644 (50–800 nM). After 72 h of treatment, MTT assays were performed as above. IC50 values were calculated using GraphPad Prism v8.0.

Cell cycle analysis

Cells were harvested 48 h post-treatment, washed in PBS, and fixed by slow dropwise addition of ice-cold 100% ethanol (final 70%) while vortexing. Samples were incubated on ice for 15 min, pelleted at 1,200 rpm for 15 min at 4°C, and resuspended in propidium iodide (PI) staining solution (50 µg/mL PI, 0.1 mg/mL RNase A, and 0.05% Triton X-100 in PBS). Samples were incubated for 40 min at 37°C in the dark, centrifuged, centrifuged, and resuspended in 100 µL PBS. Samples were analyzed using LSRFortessa flow cytometer (BD Biosciences), and cell cycle profiles were generated using FlowJo v10 (BD Biosciences). To assess the effect of CB-6644 treatment on cell cycle distribution, cells were treated for 72 h with three different concentrations (0.5×IC50, IC50, and 2×IC50) prior to fixation and analysis.

Apoptosis assay

Apoptosis was assessed using the Annexin V-FITC/PI Apoptosis Detection Kit (640914, Biolegend). Cells were harvested by trypsinization, washed twice with ice-cold PBS, and resuspended in 36 µL of Annexin V binding buffer containing 2 µL FITC-conjugated Annexin V and 4 µL propidium iodide (PI). After 15 min incubation at room temperature in the dark, 120 µL of binding buffer was added, and samples were immediately analyzed using a flow cytometer (LSRFortessa, BD Biosciences). Data were processed with FlowJo v10. The four quadrants (Q1, Q2, Q3, and Q4) are marked in all analyses. Cells positive for Annexin V only (Q3), or double positive for both Annexin V and PI (Q2) were defined as apoptotic cells (Q2 + Q3); cells positive for PI only (Q1) were defined as necrotic cells; and cells negative for both Annexin V and PI (Q4) were defined as live cells. CB-6644 treatment was applied at 0.5×IC50, IC50, and 2×IC50 concentrations for 72 h prior to analysis.

Senescence associated beta-galactosidase (SA-β-Gal) assay

Cells were seeded into 12-well plates as 20,000 cells/well and cultured for 48 h. Following two PBS washes, cells were fixed in 0.2% glutaraldehyde and 1.85% formaldehyde in PBS for 10 min at room temperature. After two additional washes with PBS, cells were incubated with SA-β-Gal staining solution (40 mM citric acid/Na phosphate buffer, 5 mM potassium ferrocyanide, 5 mM potassium ferricyanide, 150 mM NaCl, 2 mM MgCl2, 1 mg/mL X-gal in dimethylformamide) for 12 h at 37°C. SA-β-Gal–positive cells (blue staining) were imaged using a light microscope (Olympus CKX41). Quantification was performed as the percentage of SA-β-Gal–positive cells over total cells at random fields.

Wound-healing and transwell migration and invasion assays

H2052 or H2452 monolayers grown in 6-well plates were scratched with a sterile 200 µL pipette tip and washed gently with PBS to remove detached cells. Cultures were maintained in RPMI-1640 medium supplemented with 2% FBS. Wound closure was monitored microscopically (Olympus CKX41), and gap area was measured using ImageJ with the MRI_Wound_Healing_Tool. Data were reported as the percentage of wound area across independent fields. For migration, cells (5×10^4) in serum-free RPMI were seeded into the upper chambers of 8.0 µm pore Transwell inserts (353097, Falcon). The lower chamber contained RPMI with 10% FBS as chemoattractant. After 48 h incubation, non-migrated cells were removed from the upper membrane surface, and migrated cells were fixed in 3.7% formaldehyde, permeabilized in 100% methanol, and stained with 0.1% crystal violet. For invasion assays, Transwell membranes were pre-coated with 50 µL Matrigel (356234, Corning;

1:40 dilution in serum-free medium) and processed identically. Cells were imaged under a light microscope (Olympus CKX41), and cell counts were quantified using ImageJ. To evaluate the effect of CB-6644, cells were pre-treated for 72 h prior to seeding into Transwell chambers.

Two-dimensional (2D) colony formation assay

Cells were seeded at a density of 1,000 cells per well in 6-well plates and cultured for at least 10 days, with media refreshed every 3–4 days. Colonies were fixed with 3.7% formaldehyde for 10 min and stained with 0.5% crystal violet in 20% ethanol for 45 min. Plates were washed with tap water, air-dried, and imaged using the Odyssey CLx Imaging System (LI-COR). Colony area or staining intensity were quantified using ImageJ. To assess pharmacological inhibition, cells were treated with CB-6644 at 0.5×IC50, IC50, and 2×IC50 concentrations throughout the assay. Drug-containing media were replenished every 3–4 days.

Three-dimensional (3D) anchorage independent growth assay

To assess anchorage-independent growth, bottom agar layers were prepared by adding 1 mL of 0.5% noble agar (J10907, Alfa Aesar) mixed 1:1 with complete RPMI medium to each well of a 12-well plate. After solidification, cells were suspended in 0.35% noble agar (also mixed 1:1 with complete medium) at a density of 10,000 cells/mL, and overlaid onto the base agar. An additional 1 mL of medium was added on top of each well. Plates were incubated at 37°C for at least 3 weeks, with medium changed twice weekly. Colonies were visualized under 10× magnification using a light microscope (Olympus CKX41), and colony sizes were measured in random fields using ImageJ. Where indicated, CB-6644 was added to the medium at specified doses, with replenishment twice weekly.

Spheroid formation assay

To evaluate drug responses in a 3D spheroid model, cells were seeded in ultra-low attachment 96-well round-bottom plates (7007, Corning) at 5,000 cells per well in 200 µL of culture medium. Plates were centrifuged at 800 rpm for 5 min to facilitate cell aggregation [25], then incubated for 72 h to allow spheroid formation. After initial formation, 150 µL of medium was carefully removed and replaced with CB-6644 at 0.5×IC50, IC50, and 2×IC50 concentrations, with drug-containing medium replaced every 3–4 days. Spheroid morphology and size were assessed using light microscopy (Olympus CKX41), and images were analyzed with ImageJ.

Western blotting

Cells were lysed in modified RIPA Buffer [50 mM Tris pH 7.4, 150 mM NaCl, 1% Triton X-100, 0.5% Na-deoxycholate, 0.1% SDS, 1 mM EDTA, 1 mM EGTA, 10 mM β-glycerophosphate, 10 mM NaF, 1 mM PMSF, 1 mM Na-orthovanadate], supplemented with protease inhibitors (Leupeptin, Aprotinin, and Pepstatin; each at 10 µg/mL concentration). Lysates were incubated on ice for 30 min and cleared by centrifugation at maximum speed for 30 min at 4°C. Protein concentrations were determined using the Pierce BCA Protein Assay Kit (23227, Thermo Fisher Scientific). Equal amounts of protein (20 µg) were resolved by SDS-PAGE and transferred to 0.20 µm nitrocellulose membranes (10600004, GE Healthcare) via wet transfer at 350 mA for 90 min. Membranes were blocked for 1 h at room temperature in 5% (w/v) skim milk in TBS and incubated overnight at 4°C with primary antibodies (Supplementary Table 3), followed by secondary antibodies for 1 h at room temperature. Signal detection was performed using the Odyssey CLx Imaging System (LI-COR).

RNA isolation and qRT-PCR

Total RNA was extracted using the Monarch Total RNA Miniprep Kit (T2010S, NEB), following the manufacturer's instructions. For reverse transcription, 1 µg of total RNA was used per reaction with the iScript cDNA Synthesis Kit (1708891, Bio-Rad). Quantitative real-time PCR (qRT-PCR) was performed using BlasTaq™ 2X qPCR MasterMix (G891, ABM) on an Applied Biosystems 7500 Fast Real-Time PCR System. Gene expression levels were normalized to RPL41 as a reference gene using the $2^{-\Delta\Delta Ct}$ method. Primer sequences used for target amplification are listed in Supplementary Table 4.

Comet assay

Alkaline comet assays were conducted to assess DNA damage, following the protocol described [26]. Slides were pre-coated with 1% agarose and air-dried to form a thin film. Single-cell suspensions were prepared by enzymatic dissociation and centrifuged at 1,800 rpm for 2 min. A 0.4 mL aliquot of cell suspension was mixed with 1% agarose at 40°C and immediately spread onto pre-coated slides. After solidification, slides were incubated overnight at 4°C in lysis buffer (1.2 M NaCl, 100 mM Na2EDTA, 0.1% sodium lauroyl sarcosinate, 0.26 M NaOH, pH > 13) in the dark. Slides were washed twice with alkaline rinse solution (0.03 M NaOH, 2 mM Na_2EDTA) for 20 min and subjected to electrophoresis (18 V, 0.6 V/cm, 250 mA) for 25 min. DNA was stained with 10 µg/mL PI and analyzed using a fluorescence microscope. At least 50 cells per condition were quantified using the OpenComet plugin for ImageJ.

Immunofluorescence staining

Cells were seeded onto 12 mm coverslips in 24-well plates and cultured for 48 h. Cells were fixed with 3.7% formaldehyde for 10 min at room temperature and permeabilized with 0.5% Triton X-100 for 5 min on a shaker. After blocking with 5% BSA for 1 h, cells were incubated with primary antibodies against γH2AX (1/500; ab11174, Abcam), MSLN (1/200; ab196235, Abcam), Ki67 (1/200; 27309-1-AP, Proteintech), or α-Tubulin (1/200; sc-32293, Santa Cruz) for 1 h at room temperature. After PBS washes, cells were incubated with either Alexa Fluor 488 (1/500; ab150105, Abcam) or Alexa Fluor 568 (1/500; ab175470, Abcam) secondary antibodies for 1 h. Nuclei were counterstained with DAPI for 1 min and mounted with an antifade medium. Imaging was performed using a Zeiss LSM880 confocal microscope.

Histopathological analysis of primary tumor samples and tissue microarrays

For each confirmed MPM case, 4 μm sections were deparaffinized, followed by antigen retrieval performed on a Ventana Benchmark Ultra immunostainer using cell conditioning 1 (CC1) buffer from Ventana Medical Systems (Tucson, AZ), as previously described [27]. After blocking endogenous peroxidase activity, slides were incubated with pre-diluted primary antibodies against MSLN (760-4445, Ventana) and Ki-67 (790-4286, Ventana) for 32 min at 36°C. Immunoreactivity was visualized using the Opti-View Universal DAB Detection Kit (Ventana Medical Systems). Two commercially available malignant mesothelioma tissue microarrays (TMAs) MS801b and MS1001b (TissueArray, Rockville, MD), each with duplicate cores per case, were processed identically as described above. For RUVBL1 IHC, rabbit polyclonal antibody (10210-2-AP, Proteintech) was used at 1:50 dilution, with DAB detection and hematoxylin counterstain. High-resolution images were captured using an Olympus BX53 microscope equipped with 20× and 40× objectives and a DP27 digital camera.

Immunohistochemical evaluation

The scoring of IHC staining was conducted blindly, without prior knowledge of clinical information. For each core, the immunoreactive scores (IRS) were calculated by multiplying the proportion of positively stained cells (scores: 0–4) by the staining intensity (scores: 0–3) [28]. Proportion scores were assigned as follows: 0 (no staining), 1 (1–10%), 2 (11–50%), 3 (51–80%), and 4 (81–100%). Staining intensity scores were categorized as: 0 (negative), 1 (mild), 2 (moderate), and 3 (intense). IRS results were classified as no staining (0–1), mild (2–3), moderate (4–8), or strong (9–12).

CRISPR Screening and Gene Set Enrichment Analysis

CRISPR screen data and viability score computation were performed following the analytical pipeline described in a previously published genome-wide functional screen study [29]. Gene essentiality for RUVBL1, RUVBL2, and interactome genes was assessed across mesothelioma cell lines using CRISPR viability scores. Differential dependency was analyzed using context-specific z-scores, and plotted using GraphPad Prism v8.0 or R (ggplot2) for visualization. Gene effect scores, RNAi dependency data, and expression profiles were retrieved from the DepMap Public 25Q3 Release, accessed at https://depmap.org/portal/download/ [30]. To interrogate pathway-level changes associated with RUVBL1 expression, gene set enrichment analysis (GSEA) was performed using curated datasets GSE2549, GSE51024, GSE163722 and GSE29211. Each dataset was independently stratified into RUVBL1 High and RUVBL1 Low groups based on the median expression. Differentially expressed genes (DEGs) between the High and Low expression groups were identified and analyzed for enriched gene sets using the GSEA tool [31]. For each analysis, the DEG lists annotated with phenotype labels ("High" vs. "Low") were uploaded to the GSEA platform, and normalized enrichment scores (NES), nominal p-values, and false discovery rates (FDR) were computed. Parameters for GSEA included 500–1,000 phenotype permutations, and gene sets were considered significantly enriched with NES > 1, nominal p-value < 0.05, and FDR q-value < 0.25. Dot plots and enrichment plots were generated using custom R scripts and ggplot2 to visualize top-enriched pathways.

Statistical analysis

Data are presented as mean ± SEM or mean ± SD, as specified in the figure legends. For comparisons between two independent groups, either Student's t-test or multiple t-tests were employed. For multiple group comparisons, one-way or two-way analysis of variance (ANOVA) was applied. To correct for multiple testing, statistical significance was assessed using the Two-Stage Linear Step-Up Procedure of Benjamini, Krieger, and Yekutieli. All analyses were conducted using GraphPad Prism version 8.0 (GraphPad Software, San Diego, USA). A p-value < 0.05 was considered statistically significant, with significance levels defined as *p < 0.05, **p < 0.01, and ***p < 0.001.

RESULTS

An integrated prioritization framework identifies RUVBL1 as a non-redundant dependency in MPM

To chart a therapeutically exploitable landscape of molecular liabilities in malignant pleural mesothelioma (MPM), we performed a post hoc reanalysis of our genome-scale CRISPR dropout screens [29]. We implemented a stringent tri-parametric prioritization framework designed to filter biologically coherent dependencies over noise-prone hits which required candidates to exhibit: (i) recurrent essentiality in two independent MPM cell lines, H2052 and H2452, defined by a CRISPR Viability Score < –3.0 with false discovery rate (FDR)-adjusted p-value < 0.02; (ii) catalytically competent enzymatic activity amenable to direct inhibition; and (iii) pharmacologic tractability, inferred from chemogenomic annotations, including the canSAR database [32]. This strategy returned 85 genes whose loss conferred shared essentiality in both models (Fig. 1A and 1B, Supplementary Table 5). Of these, 25 genes mapped to major enzymatic classes linked to canonical or emerging cancer hallmarks with clinical relevance (Fig. 1B and 1C), including mediators of DNA replication and genome surveillance (e.g., MCM3, MCM7, POLR3B, PRMT5), protein homeostasis (e.g., VARS, HSPA5, VCP, PSMA5), and metabolic or signaling nodes (e.g., ALG11, FNTA, HMGCS1) (Fig. 1C). Importantly, 16 of these 25 enzymes met druggability criteria (Fig. 1A and 1C), defining a tractable vulnerability network in MPM.

Within this *a priori* selection framework, the AAA+ ATPase RUVBL1 emerged as the top-ranking candidate (Fig. 1C). RUVBL1 disruption caused a profound reduction in CRISPR viability scores across both cell lines (Fig. S1A), with each of four independent gRNAs reducing fitness by at least 50% (Fig. 1D), exceeding widely used thresholds for cancer essential genes [33]. Benchmarking our results for generalizability against the Cancer Dependency Map (DepMap) confirmed RUVBL1 as pan-essential across the MPM cell line cohort (Fig. 1E and S1B). This finding is supported by its uniformly high expression in the Cancer Cell Line Encyclopedia (CCLE) transcriptomic profiles (Fig. 1F), a pattern typical of genes under positive selection for sustained oncogenic function [34]. Analysis of TCGA MPM RNA-seq data using the Gene Set Cancer Analysis (GSCA) platform [35], further revealed that *RUVBL1* upregulation is driven by focal copy number gains and locus-specific hypomethylation (Fig. S1C), suggesting a multimodal basis for its dysregulation. To authenticate RUVBL1 as a bona fide liability, we performed time-resolved competitive proliferation assays in H2052 and H2452 cells. Upon CRISPR gene knockout, RUVBL1-deleted populations displayed progressive growth deficits compared with gRen controls, as monitored by flow cytometry tracking of a Venus fluorescent reporter (Fig. 1G). The temporal nature of this phenotype argues for a durable

loss-of-fitness effect rather than a transient proliferative delay, in line with on-target perturbation of an essential component of the MPM survival circuitry.

RUVBL1/2 assemblies operate as an obligate survival hub

RUVBL1 functions as an obligate heterohexamer with its paralog RUVBL2, forming the catalytic core of several nuclear multiprotein complexes, including the R2TP/PAQosome, INO80, and TIP60 complexes. These assemblies integrate chromatin remodeling, transcriptional control, DNA repair, and ribonucleoprotein biogenesis into a coordinated regulatory network [13]. Consistent with this functional paradigm, we found that RUVBL2 was highly expressed across MPM models (Fig. S1D), and its depletion phenocopied the fitness defects of RUVBL1 loss (Fig. S1E-G). Expanding this analysis to the broader interactome, we observed that genetic inactivation of other subunits within RUVBL1/2-nucleated complexes conferred consensual reductions in CRISPR viability scores (Fig. S2A) and DepMap gene effect scores (Fig. S2B). These data posit a model of network-level addiction on this structural and regulatory interactome (Fig. S2C), in which RUVBL1/2-based assemblies operate as dynamic molecular hubs essential for survival and stress-adaptive states. Consequently, perturbation of individual subunits appears sufficient to destabilize the integrity of the entire multiprotein module.

RUVBL1 is upregulated in mesothelioma and stratifies clinical outcomes

To contextualize these findings clinically, we interrogated large-scale transcriptomic cohorts and tissue microarrays (TMAs). *RUVBL1* mRNA levels were significantly elevated in primary MPM tumors compared to benign mesothelial or lung tissues (GSE42977), and in mesothelioma cell lines relative to stromal populations (GSE117668) (Fig. 1H). Crucially, high RUVBL1 expressing tumors were enriched for mesothelioma-defining transcriptional signatures (Fig. S2D), linking RUVBL1 to disease-specific pathophysiology. At the protein level, immunohistochemical analysis of TMAs comprising 26 MPM cases, 46 mesotheliomas or solid cancers from peritoneum, omentum, pericardium, and other sites, together with 11 normal or benign mesothelial controls, confirmed prominent cytoplasmic and perinuclear RUVBL1 staining in tumors, with heterogeneous immunoreactivity scores (IRS 0-12) (Fig. 1I and Fig. S3A). The majority of tumors exhibited mild (IRS 2–3) to strong (IRS 9–12) RUVBL1 abundance, whereas benign mesothelium showed minimal or no reactivity (IRS 0-1) (Fig. 1I and 1J). Notably, unlike certain alterations that occur exclusively in specific tissue lineages [36], aberrant RUVBL1 expression was unified across anatomically and histologically distinct

mesothelioma subtypes (Fig. 1I, Fig. S3A and S3B), a pattern defining a pan-mesothelioma molecular signature rather than a subtype-restricted phenomenon. To evaluate the prognostic trajectory, we performed Kaplan–Meier analyses of the TCGA MPM cohort using UALCAN and cSurvival platforms [37,38]. High *RUVBL1* expression or copy number gains, but not differential methylation at the locus, significantly correlated with inferior overall survival (Fig. 1K, Fig. S4A and S4B). Analogous clinical trends were observed for its paralog *RUVBL2* (Fig. S4C and S4D). Collectively, these data establish RUVBL1, and by extension the entire RUVBL1/2-nucleated machinery, as a biologically essential and clinically adverse fitness dependency in MPM.

RUVBL1 depletion triggers DNA replication stress and checkpoint engagement

To deconvolute the mechanistic basis of this dependency, we characterized the cellular consequences of CRISPR-mediated RUVBL1 ablation in H2052 and H2452 cells (Fig. 2A). RUVBL1 depletion severely attenuated growth kinetics (Fig. S5A), and suppressed nascent DNA synthesis, as quantified by BrdU incorporation (Fig. 2B and S5B). This cytostatic effect manifested as a loss of long-term clonogenic capacity in two-dimensional (2D) adherent monolayers (Fig. 2C and 2D), and abolished anchorage-independent growth in three-dimensional (3D) spheroid models (Fig. 2E and 2F). Importantly, ectopic expression of a CRISPR-resistant RUVBL1 cDNA harboring synonymous mutations within the gRNA recognition site (mRUVBL1) fully rescued clonogenic outgrowth (Fig. 2G and 2H, Fig. S5C), confirming on-target specificity.

Cell cycle profiling revealed that RUVBL1 loss precipitated context-dependent checkpoint engagement. Specifically, RUVBL1-deficient H2052 cells accumulated in G2/M phase, whereas H2452 cells exhibited a defect in S-phase progression (Fig. 2I). This was accompanied by the induction of the cyclin-dependent kinase (CDK) inhibitor p21 (*CDKN1A*) (Fig. 2J), a canonical effector of DNA damage–induced arrest [39], and the acquisition of senescence biomarkers, including enlarged morphology and senescence-associated β-galactosidase (SA-β-Gal) activity (Fig. 2K and 2L). In an effort to expose transcriptomic modulation by RUVBL1, we performed unbiased gene set enrichment analysis (GSEA). *RUVBL1* expression in patient cohorts correlated positively with MYC and E2F targets and G2/M checkpoint signatures (Fig. 2M, Fig. S6A-C). Thus, these data reinforce RUVBL1's role as a central node in the proliferative network of MPM.

RUVBL1 maintains genome integrity by stabilizing the PIKK kinases ATM and ATR

The profound cell cycle perturbations combined with previous reports implicating RUVBL1 in replication fork stabilization and genome surveillance [18], prompted us to explore whether its loss compromises DNA replication and damage responses. Cells lacking RUVBL1 exhibited signs of acute replication stress, including intense nuclear accumulation of γH2AX (Fig. 3A and 3B), a phosphorylated histone variant marking DNA double-strand breaks and stalled replication forks [40], which was further corroborated by western blotting (Fig. 3C). Alkaline comet assays also demonstrated a substantial increase in comet tail moments following RUVBL1 depletion (Fig. 3D and 3E), consistent with extensive DNA fragmentation and unresolved genotoxic stress [41].

Since the phosphoinositide 3-kinase-related kinases (PIKK) ATM and ATR require the RUVBL1/2 complex and the HSP90–R2TP/TTT (PAQosome) chaperone for proper maturation and stability [39,40], we hypothesized that its loss compromises the stability of PIKK family kinases essential for the DNA damage response. Indeed, RUVBL1 depletion resulted in a marked reduction of total ATM and ATR protein levels (Fig. 3F). Further supporting the interpretation that RUVBL1 operates within a coordinated genome-maintenance network, transcriptomic analyses of primary MPM tumors identified positive correlations between RUVBL1 and gene programs involved in DNA damage repair and replication (Fig. 3G). As expected, the unresolved genotoxic stress in RUVBL1-depleted cells culminated in apoptotic cell death, evidenced by Annexin V positivity (Fig. 3H and Fig. S7), and PARP cleavage (Fig. 3I), a signature product of suicidal proteases like caspases [42]. Together, these results suggest that RUVBL1 acts as a guardian of genome stability, required to sustain the high replication fidelity demanded by MPM cells.

Ectopic RUVBL1 expression fuels EMT and invasive plasticity

RUVBL1 has been linked to migratory and invasive behaviors across multiple solid malignancies [43,44]. We thus investigated whether RUVBL1 drives aggressive phenotypes in MPM. To assess this dimension, we deployed wound-healing (scratch) assays in H2052 and H2452 monolayer cultures, enabling evaluation of collective migration and single-cell motility. RUVBL1 loss significantly impaired collective migration, with delayed wound closure compared to gRen controls (Fig. 4A and 4B), abolished chemotactic migration through porous membranes (Fig. 4C and 4D), and eroded invasion capacity to traverse extracellular matrix barriers (Fig. 4E and 4F).

To test whether gain-of-function activity of RUVBL1 was able to amplify these phenotypes, we next engineered H2052 and H2452 cell lines with ectopic RUVBL1 expression (Fig. 5A). As expected, these clones displayed higher proliferative kinetics, as shown by increased BrdU indices (Fig. 5B and Fig. S8A), and enhanced anchorage-independent spheroid growth in soft agar, generating more and larger colonies (Fig. 5C and 5D). Strikingly, RUVBL1 overexpression induced overt morphological changes consistent with mesenchymal-like transformation (Fig. S8B). In H2052 cells, this shift manifested as a discernible transition from cobblestone-like epithelial morphology to elongated, spindle-shaped contours characteristic of mesenchymal cells, while both cell lines developed extensive actin-rich membrane protrusions (Fig. 5E), indicative of cytoskeletal reorganization. Functionally, these changes translated into enhanced migration (Fig. 5F and Fig. S8C) and invasion (Fig. 5G and 5H).

Given these adaptations, we hypothesized that RUVBL1 engages epithelial-to-mesenchymal transition (EMT), a phenotypic program driving cancer progression, therapeutic resistance, and metastasis [45]. Indeed, RUVBL1 overexpression suppressed epithelial markers, *CDH1* (E-cadherin) and *OCLN* (Occludin), while inducing mesenchymal drivers, *CDH2* (N-cadherin) and *VIM* (Vimentin), in H2052 cells (Fig. 5I). These transcriptional changes were paralleled at the protein level by increased Vimentin and N-cadherin (Fig. 5J). Consistent with the activation of an EMT-like program, transcription factors associated with EMT were also upregulated in RUVBL1 overexpressing cells (Fig. 5K). Interestingly, despite adopting clear morphological shifts, H2452 cells did not show consistent modulation of canonical EMT signatures (Fig. S8D and S8E), suggesting that the propensity to execute a full EMT program may depend on cell line-specific factors. Nevertheless, these observations are in agreement with previous reports identifying RUVBL1 as a modulator of EMT-related gene expression in other epithelial malignancies [46]. Furthermore, patient transcriptomes revealed strong correlations between RUVBL1 and mesenchymal gene signatures (Figure 5L), providing a clinical relevance for this relationship. Together, these data extend the function of RUVBL1 beyond proliferation, underscoring its driver role in phenotypic plasticity and reprogramming toward mesenchymal states.

Small-molecule inhibition phenocopies genetic ablation

Having established RUVBL1 as a non-redundant essentiality, we interrogated its druggability using CB-6644, a highly selective allosteric inhibitor that stabilizes the RUVBL1/2 heterohexamer in an ADP-bound inactive conformation, thereby arresting its ATPase cycle

[47,48]. Structural modeling using the canSAR chemogenomic platform confirmed the accessibility of the drug-binding pocket (Fig. 6A). Exposure of H2052 and H2452 cells to CB-6644 resulted in a potent, dose-dependent suppression of viability with low-nanomolar IC50 values (Fig. 6B). This anti-proliferative effect was driven by an acute blockade of DNA replication (Fig. 6C and Fig. S9A), which translated into a durable loss of clonogenic capacity in adherent monolayers (Fig. S9B and S9C), and abolished anchorage-independent growth in 3D spheroid cultures (Fig. 6D and 6E).

Critically, pharmacological inhibition faithfully recapitulated the specific molecular fingerprints of RUVBL1 genetic knockout. Cell cycle profiling demonstrated a lineage-specific arrest upon CB-6644 exposure. In particular, H2052 cells accumulated at G2/M, whereas H2452 cells stalled in S phase (Fig. 6F and Fig. S9D), accompanied by dose-dependent upregulation of p21 (Fig. 6G), consistent with checkpoint activation and enforced cytostasis in other settings [49]. At the molecular level, ATPase inhibition triggered a canonical replication stress response, marked by the extensive accumulation of γH2AX (Fig. 6H), and the concomitant destabilization of ATM and ATR proteins (Fig. 6I). This confirms that catalytic inhibition of the RUVBL1/2 complex is sufficient to collapse the replication fork protection machinery. Consequently, drug exposure culminated in apoptosis, evidenced by PARP cleavage and Annexin V positivity (Fig. 6J and Fig. S9E). The cytotoxic effects were more pronounced in cells undergoing G2/M arrest, suggesting that CB-6644 may exploit a particular vulnerability state in the cell cycle.

Furthermore, CB-6644 effectively neutralized aggressive phenotypes. Transwell migration assays revealed a marked reduction in cell motility across porous membranes (Fig. 6K and 6L), and Matrigel invasion assays demonstrated near-complete loss of matrix penetration following treatment (Fig. 6M and 6N). These data provide proof-of-concept that small-molecule targeting of the RUVBL1/2 ATPase provides strong therapeutic effects by exploiting the replication stress vulnerability of MPM.

Patient-derived, treatment-naïve MPM models exhibit sensitivity to RUVBL1 targeting

To rigorously validate the translational relevance of our findings, we moved beyond established cell lines to patient-derived, treatment-naïve primary mesothelioma cultures (MPM-TPCs). Such *ex vivo* systems [50,51], when successfully generated from surgically resected pleural tumors (Fig. 7A), may offer a high-fidelity platform that preserves the genetic heterogeneity and histological architecture of the parental disease. To this end, we established two

independent models: MPM-TPC-D1 (biphasic histology) and MPM-TPC-D2 (epithelioid histology), both originating from patients with documented asbestos exposure (Fig. 7B). Histological characterization confirmed key diagnostic hallmarks of mesothelioma (Fig. 7B), including robust expression of Mesothelin (MSLN), a clinically validated marker elevated in more than 80% of tumors [52], and high Ki-67 indices (MPM-Tumor-D1: 44% and MPM-Tumor-D2: 62%) (Fig. 7C), reflecting strong proliferative activity [53,54]. Importantly, both tumors showed high basal levels of RUVBL1 expression (Fig. 7C).

When propagated as adherent monolayers, MPM-TPCs recapitulated the phenotype of their respective tumors, exhibiting cobblestone-like epithelial morphology with subtype-associated heterogeneity (Fig. 7D). Importantly, the patterns of MSLN expression, Ki-67 positivity (50% for D1, 71.4% for D2), and RUVBL1 expression, were retained *in vitro* (Fig. 7E-G), validating these cultures as clinically relevant platforms for pharmacologic interrogation.

Treatment of these patient-proximal models with CB-6644 elicited a profound dose-dependent cytotoxicity (Fig. 8A). While the IC50 values were moderately higher than those observed in long-term established cell lines, a phenomenon consistent with enhanced stress-buffering capacity and inherent drug tolerance in primary isolates [55,56], the therapeutic window remained significant. Mechanistically, CB-6644 treatment effectively halted nascent DNA synthesis (Fig. 8B and C), and abolished long-term clonogenic survival (Fig. 8D and E). Consistent with acute replication checkpoint activation, drug exposure induced a convergent S-phase arrest (Fig. 8F), and triggered apoptotic cell death marked by PARP cleavage (Fig. 8G). In assays modeling higher-order tumorigenic phenotypes [57], CB-6644 disrupted scaffold-free spheroid self-assembly and expansion of patient-derived models (Fig. 8H and I), and effectively blocked invasion through extracellular matrix barriers (Fig. 8J and K). These preclinical data demonstrate that RUVBL1 dependency is not an artifact of *in vitro* culture adaptation, but a fundamental, pharmacologically exploitable vulnerability conserved across diverse histological subtypes of human mesothelioma.

Discussion

Malignant pleural mesothelioma (MPM) represents a persistent clinical challenge, characterized by a distinct paucity of actionable drivers, therapeutic recalcitrance and modest survival benefits even with aggressive multimodal strategies and modern immunotherapeutic interventions [58]. While recent CRISPR-based functional genomic efforts have begun to map the dependency landscape of this malignancy, highlighting essential genes in cell cycle control

and chromatin regulation [29,59–61], identifying vulnerabilities that are both distinct from canonical oncogenic functions and therapeutically exploitable underscores the need for continuous efforts. Within this evolving framework, our work uncovers the evolutionarily conserved AAA+ ATPase RUVBL1 as a critical non-oncogene addiction in MPM. Although RUVBL1 is rarely mutated or amplified in MPM [62], our data show that MPM cells hijack this essential machinery to sustain their high-stress oncogenic state. The robust correlation between elevated RUVBL1 expression and shortened patient survival underscores that this co-option is not merely a bystander effect but a driver of aggressive disease biology. These observations extend the emerging paradigm of targeting housekeeping cellular machines in cancer, aligning with recent evidence that the Achilles' heels of mesothelioma often reside in stress-response and chromatin-regulatory modules rather than in canonical kinase drivers [61].

Mechanistic interpretation of this dependency points to RUVBL1's centrality in fundamental processes that cancer cells must hyperactivate. As an obligate component of the TIP60/NuA4 histone acetyltransferase and INO80/SWR1 chromatin remodeling complexes [13,63], RUVBL1 orchestrates the epigenetic plasticity required for transcription, DNA replication, and repair [18,64]. Furthermore, its function within the R2TP co-chaperone system is indispensable for the assembly and maturation of PIKK family kinases, including ATM, ATR, and mTOR [65–68]. Indeed, we observe that RUVBL1 ablation in MPM cells precipitates a rapid accumulation of DNA damage, cell cycle collapse, and apoptosis. This phenotype signifies a catastrophic failure of genome maintenance programs and an inability to buffer proteotoxic stress and replicative stress inherent to the malignant state. Our findings resonate with the oncogene-induced stress model, where tumors with elevated replication loads are selectively hypersensitive to the disruption of chaperone networks, whereas normal cells can tolerate their partial inhibition [18,69]. Given that mesotheliomas are driven by extensive chromosomal rearrangements and asbestos-induced oxidative DNA damage, they are uniquely vulnerable to the disruption of RUVBL1-driven homeostatic functions. We propose that the concurrent attenuation of DNA repair capacity and growth-promoting gene expression creates a lethal double hit, rendering cells unable to resolve genotoxic insults or sustain cycling, which explains the profound apoptosis observed upon RUVBL1 knockdown.

Beyond genome integrity, our data suggest that RUVBL1 underpins the transcriptional circuitry essential for mesothelioma growth and phenotypic plasticity. Our integrative transcriptomic profiling revealed a tight co-regulation of RUVBL1 with cell cycle and DNA replication/repair networks, indicating that RUVBL1 sustains a broad oncogenic transcriptional output. This

mirrors dependencies observed in other transcriptionally driven cancers, such as Ewing sarcoma and pancreatic ductal adenocarcinoma, where RUVBL1 is indispensable for maintaining MYC-driven programs [63,70,71]. It is tempting to speculate that a similar axis operates in mesothelioma, wherein RUVBL1 stabilizes the chromatin binding of key transcription factors to maintain the high protein synthesis and proliferation rates characteristic of this malignancy. Indeed, recent work has shown that KLF5 recruits RUVBL1/2 as chromatin coactivators to orchestrate divergent programs in pancreatic cancer [72], linking these ATPases to dynamic transcriptional rewiring and lineage plasticity [73]. This aligns with our observation that RUVBL1 overexpression fuels an EMT phenotype in MPM. Thus, RUVBL1 depletion does not simply arrest the cell cycle; it disrupts the transcriptional machinery required for aggressive dissemination, suggesting that this axis stabilizes oncogenic chromatin states essential for aggressive states [72].

Despite the scarcity of canonical oncogenic mutations in MPM [36,74,75], the identification of RUVBL1 as a vulnerability in MPM enriches the theme that chromatin remodelers and co-chaperones represent high-value targets in this disease [29,59,61]. Similar dependencies have been noted in non-small cell lung cancer, multiple myeloma, and neuroblastoma, where cells exhibit high sensitivity to RUVBL1/2 inhibition, suggesting a pan-cancer relevance [18,47,76–78]. Unlike pathway-specific inhibition, targeting a structural hub like RUVBL1 exerts pleiotropic anti-tumor effects, simultaneously dampening multiple pro-tumorigenic signals. This multi-pronged impact is evident in our results, where RUVBL1 suppression phenocopied the combined disruption of several cancer hallmarks simultaneously.

These mechanistic insights carry direct and immediate translational implications. Although targeting a ubiquitous ATPase raises concerns regarding toxicity, accumulating evidence indicates a viable therapeutic window for RUVBL1/2 blockade. Cancer cells appear to be more reliant on RUVBL1-mediated buffering of oncogenic stress than normal tissues. Small-molecule inhibitors of RUVBL1/2 ATPase activity have already demonstrated promising anti-tumor activity in preclinical models [47,79–81]. The allosteric compound CB-6644, for example, selectively binds the RUVBL1/2 complex, inhibiting its ATPase function and suppressing tumor xenograft growth, while other agents induce DNA damage, apoptosis, and downregulation of oncogenic transcription [18,82]. Furthermore, we envision that rational combination strategies pairing RUVBL1/2 inhibition with DNA-damaging chemotherapy or radiotherapy could be particularly effective by disabling the tumor's ability to repair induced damage [69,83]. Specifically, since loss of the BAP1 tumor suppressor perturbs chromatin

homeostasis, tumors with BAP1 inactivation might exhibit synthetic lethality with RUVBL1 blockade, a hypothesis that warrants priority investigation. Additionally, given emerging evidence that RUVBL1/2 shapes inflammatory and immune programs [76,84], RUVBL1-directed therapy could potentially reprogram the mesothelioma immune microenvironment, sensitizing these tumors to immune checkpoint blockade [8,9]. Finally, the continued use of patient-derived organoid models will be crucial for dissecting interpatient heterogeneity and benchmarking these combinations against standard-of-care regimens [85–87].

In conclusion, we present RUVBL1 as an actionable Achilles' heel of MPM. By integrating functional genomics, multi-omic profiling, and pharmacologic perturbation, we delineate a RUVBL1/2-centered network that links replication stress signaling to tumor cell fitness and phenotypic plasticity. Most critically, allosteric inhibition effectively collapses this network in established cell lines and patient-derived models. These findings nominate RUVBL1 and, by extension, the RUVBL1/2 complex as a promising therapeutic entry point, providing a conceptual and preclinical framework for strategies aimed at exploiting this dependency in MPM.

Acknowledgements

This work was supported by grants from the Scientific and Technological Research Council of Türkiye (TÜBİTAK, Project No: 221Z170) and Dokuz Eylul University, Department of Scientific Research Projects (Project No: TSA-2024-3353). The authors acknowledge Izmir Biomedicine and Genome Center (IBG) for providing financial and administrative support. We also thank the Flow Cytometry and Cell Sorting, Optical Imaging, and research support units at IBG.

Contributions

M.Z.G. conducted experiments, performed data analysis, drafted the manuscript and figures. E.C. provided preliminary data, helped establish the primary cultures, conducted experiments, generated figures, and assisted in manuscript preparation. S.E. performed experiments, analyzed public datasets, generated relevant plots and figures, and contributed to manuscript preparation. M.O. established primary cultures, performed experiments, generated figures, and assisted in manuscript preparation. Z.B. performed pathological evaluation, interpreted clinical samples, and validated experimental findings. B.A. conducted inhibitor-based experiments. G.O.S., V.K., and E.S.U. provided clinical guidance, facilitated sample acquisition, and

managed patient data. S.S. secured funding, supervised the experiments and data analysis, and wrote the manuscript. All authors reviewed and approved the final version of the manuscript.

Competing Interests

The authors declare no potential competing interests.

Data Availability

The authors declare that all data supporting the findings of this study are available within the article and its Supplementary Information. Detailed initial results of the CRISPR screen were previously reported in Cakiroglu *et al.* [29]. CRISPR screening data are also available from the corresponding author upon reasonable request.

References

1. Sauter, J.L.; Dacic, S.; Galateau-Salle, F.; Attanoos, R.L.; Butnor, K.J.; Churg, A.; Husain, A.N.; Kadota, K.; Khoor, A.; Nicholson, A.G.; et al. The 2021 WHO Classification of Tumors of the Pleura: Advances Since the 2015 Classification. *J. Thorac. Oncol. Off. Publ. Int. Assoc. Study Lung Cancer* **2022**, *17*, 608–622, doi:10.1016/j.jtho.2021.12.014.

2. Scherpereel, A.; Wallyn, F.; Albelda, S.M.; Munck, C. Novel Therapies for Malignant Pleural Mesothelioma. *Lancet Oncol.* **2018**, *19*, e161–e172, doi:10.1016/S1470-2045(18)30100-1.

3. Robinson, B.W.S.; Musk, A.W.; Lake, R.A. Malignant Mesothelioma. *Lancet Lond. Engl.* **2005**, *366*, 397–408, doi:10.1016/S0140-6736(05)67025-0.

4. Dacic, S. Pleural Mesothelioma Classification-Update and Challenges. *Mod. Pathol. Off. J. U. S. Can. Acad. Pathol. Inc* **2022**, *35*, 51–56, doi:10.1038/s41379-021-00895-7.

5. Papa, S.; Popat, S.; Shah, R.; Prevost, A.T.; Lal, R.; McLennan, B.; Cane, P.; Lang-Lazdunski, L.; Viney, Z.; Dunn, J.T.; et al. Phase 2 Study of Sorafenib in Malignant Mesothelioma Previously Treated with Platinum-Containing Chemotherapy. *J. Thorac. Oncol. Off. Publ. Int. Assoc. Study Lung Cancer* **2013**, *8*, 783–787, doi:10.1097/JTO.0b013e31828c2b26.

6. Nowak, A.K.; Millward, M.J.; Creaney, J.; Francis, R.J.; Dick, I.M.; Hasani, A.; van der Schaaf, A.; Segal, A.; Musk, A.W.; Byrne, M.J. A Phase II Study of Intermittent Sunitinib Malate as Second-Line Therapy in Progressive Malignant Pleural Mesothelioma. *J. Thorac. Oncol. Off. Publ. Int. Assoc. Study Lung Cancer* **2012**, *7*, 1449–1456, doi:10.1097/JTO.0b013e31825f22ee.

7. Scagliotti, G.V.; Gaafar, R.; Nowak, A.K.; Nakano, T.; van Meerbeeck, J.; Popat, S.; Vogelzang, N.J.; Grosso, F.; Aboelhassan, R.; Jakopovic, M.; et al. Nintedanib in Combination with Pemetrexed and Cisplatin for Chemotherapy-Naive Patients with Advanced Malignant Pleural Mesothelioma (LUME-Meso): A Double-Blind, Randomised, Placebo-Controlled Phase 3 Trial. *Lancet Respir. Med.* **2019**, *7*, 569–580, doi:10.1016/S2213-2600(19)30139-0.

8. Yap, T.A.; Nakagawa, K.; Fujimoto, N.; Kuribayashi, K.; Guren, T.K.; Calabrò, L.; Shapira-Frommer, R.; Gao, B.; Kao, S.; Matos, I.; et al. Efficacy and Safety of Pembrolizumab in Patients with Advanced Mesothelioma in the Open-Label, Single-Arm, Phase 2 KEYNOTE-158 Study. *Lancet Respir. Med.* **2021**, *9*, 613–621, doi:10.1016/S2213-2600(20)30515-4.

9. Popat, S.; Curioni-Fontecedro, A.; Dafni, U.; Shah, R.; O'Brien, M.; Pope, A.; Fisher, P.; Spicer, J.; Roy, A.; Gilligan, D.; et al. A Multicentre Randomised Phase III Trial Comparing Pembrolizumab versus Single-Agent Chemotherapy for Advanced Pre-Treated Malignant Pleural Mesothelioma: The European Thoracic Oncology Platform (ETOP 9-15) PROMISE-Meso Trial. *Ann. Oncol. Off. J. Eur. Soc. Med. Oncol.* **2020**, *31*, 1734–1745, doi:10.1016/j.annonc.2020.09.009.

10. Ledermann, J.; Harter, P.; Gourley, C.; Friedlander, M.; Vergote, I.; Rustin, G.; Scott, C.; Meier, W.; Shapira-Frommer, R.; Safra, T.; et al. Olaparib Maintenance Therapy in Platinum-Sensitive Relapsed Ovarian Cancer. *N. Engl. J. Med.* **2012**, *366*, 1382–1392, doi:10.1056/NEJMoa1105535.

11. Morschhauser, F.; Tilly, H.; Chaidos, A.; McKay, P.; Phillips, T.; Assouline, S.; Batlevi, C.L.; Campbell, P.; Ribrag, V.; Damaj, G.L.; et al. Tazemetostat for Patients with Relapsed or Refractory Follicular Lymphoma: An Open-Label, Single-Arm, Multicentre, Phase 2 Trial. *Lancet Oncol.* **2020**, *21*, 1433–1442, doi:10.1016/S1470-2045(20)30441-1.

12. DiNardo, C.D.; Stein, E.M.; de Botton, S.; Roboz, G.J.; Altman, J.K.; Mims, A.S.; Swords, R.; Collins, R.H.; Mannis, G.N.; Pollyea, D.A.; et al. Durable Remissions with Ivosidenib in IDH1-Mutated Relapsed or Refractory AML. *N. Engl. J. Med.* **2018**, *378*, 2386–2398, doi:10.1056/NEJMoa1716984.

13. Dauden, M.I.; López-Perrote, A.; Llorca, O. RUVBL1-RUVBL2 AAA-ATPase: A Versatile Scaffold for Multiple Complexes and Functions. *Curr. Opin. Struct. Biol.* **2021**, *67*, 78–85, doi:10.1016/j.sbi.2020.08.010.

14. Willhoft, O.; Wigley, D.B. INO80 and SWR1 Complexes: The Non-Identical Twins of Chromatin Remodelling. *Curr. Opin. Struct. Biol.* **2020**, *61*, 50–58, doi:10.1016/j.sbi.2019.09.002.

15. Bizarro, J.; Dodré, M.; Huttin, A.; Charpentier, B.; Schlotter, F.; Branlant, C.; Verheggen, C.; Massenet, S.; Bertrand, E. NUFIP and the HSP90/R2TP Chaperone Bind the SMN Complex and Facilitate Assembly of U4-Specific Proteins. *Nucleic Acids Res.* **2015**, *43*, 8973–8989, doi:10.1093/nar/gkv809.

16. Jha, S.; Gupta, A.; Dar, A.; Dutta, A. RVBs Are Required for Assembling a Functional TIP60 Complex. *Mol. Cell. Biol.* **2013**, *33*, 1164–1174, doi:10.1128/MCB.01567-12.

17. Wong, M.M.; Cox, L.K.; Chrivia, J.C. The Chromatin Remodeling Protein, SRCAP, Is Critical for Deposition of the Histone Variant H2A.Z at Promoters. *J. Biol. Chem.* **2007**, *282*, 26132–26139, doi:10.1074/jbc.M703418200.

18. Yenerall, P.; Das, A.K.; Wang, S.; Kollipara, R.K.; Li, L.S.; Villalobos, P.; Flaming, J.; Lin, Y.-F.; Huffman, K.; Timmons, B.C.; et al. RUVBL1/RUVBL2 ATPase Activity

Drives PAQosome Maturation, DNA Replication and Radioresistance in Lung Cancer. *Cell Chem. Biol.* **2020**, *27*, 105-121.e14, doi:10.1016/j.chembiol.2019.12.005.

19. Haurie, V.; Ménard, L.; Nicou, A.; Touriol, C.; Metzler, P.; Fernandez, J.; Taras, D.; Lestienne, P.; Balabaud, C.; Bioulac-Sage, P.; et al. Adenosine Triphosphatase Pontin Is Overexpressed in Hepatocellular Carcinoma and Coregulated with Reptin through a New Posttranslational Mechanism. *Hepatol. Baltim. Md* **2009**, *50*, 1871–1883, doi:10.1002/hep.23215.

20. Sun, Q.; Li, F.; Yu, S.; Zhang, X.; Shi, F.; She, J. Pontin Acts as a Potential Biomarker for Poor Clinical Outcome and Promotes Tumor Invasion in Hilar Cholangiocarcinoma. *BioMed Res. Int.* **2018**, *2018*, 6135016, doi:10.1155/2018/6135016.

21. Xue, R.; Wang, Y.; Luo, X.; Zhang, H.; Guan, D.; Shi, S.; Wang, Y. Profiling of RUVBL2-Induced Transcriptome Alterations Highlights a Critical Role for Chromatin Remodeling in Ovarian Cancer. *BioFactors Oxf. Engl.* **2025**, *51*, e70041, doi:10.1002/biof.70041.

22. Zhang, G.; Wang, F.; Li, S.; Cheng, K.-W.; Zhu, Y.; Huo, R.; Abdukirim, E.; Kang, G.; Chou, T.-F. Discovery of Small-Molecule Inhibitors of RUVBL1/2 ATPase. *Bioorg. Med. Chem.* **2022**, *62*, 116726, doi:10.1016/j.bmc.2022.116726.

23. Senturk, S.; Shirole, N.H.; Nowak, D.G.; Corbo, V.; Pal, D.; Vaughan, A.; Tuveson, D.A.; Trotman, L.C.; Kinney, J.B.; Sordella, R. Rapid and Tunable Method to Temporally Control Gene Editing Based on Conditional Cas9 Stabilization. *Nat. Commun.* **2017**, *8*, 14370, doi:10.1038/ncomms14370.

24. Dayanc, B.; Eris, S.; Gulfirat, N.E.; Ozden-Yilmaz, G.; Cakiroglu, E.; Coskun Deniz, O.S.; Karakülah, G.; Erkek-Ozhan, S.; Senturk, S. Integrative Multi-Omics Identifies AP-1 Transcription Factor as a Targetable Mediator of Acquired Osimertinib Resistance in Non-Small Cell Lung Cancer. *Cell Death Dis.* **2025**, *16*, 414, doi:10.1038/s41419-025-07711-z.

25. Shi, H.; Rath, E.M.; Lin, R.C.Y.; Sarun, K.H.; Clarke, C.J.; McCaughan, B.C.; Ke, H.; Linton, A.; Lee, K.; Klebe, S.; et al. 3-Dimensional Mesothelioma Spheroids Provide Closer to Natural Pathophysiological Tumor Microenvironment for Drug Response Studies. *Front. Oncol.* **2022**, *12*, 973576, doi:10.3389/fonc.2022.973576.

26. Olive, P.L.; Banáth, J.P. The Comet Assay: A Method to Measure DNA Damage in Individual Cells. *Nat. Protoc.* **2006**, *1*, 23–29, doi:10.1038/nprot.2006.5.

27. Einama, T.; Kamachi, H.; Nishihara, H.; Homma, S.; Kanno, H.; Ishikawa, M.; Kawamata, F.; Konishi, Y.; Sato, M.; Tahara, M.; et al. Importance of Luminal Membrane Mesothelin Expression in Intraductal Papillary Mucinous Neoplasms. *Oncol. Lett.* **2015**, *9*, 1583–1589, doi:10.3892/ol.2015.2969.

28. Remmele, W.; Stegner, H.E. [Recommendation for uniform definition of an immunoreactive score (IRS) for immunohistochemical estrogen receptor detection (ER-ICA) in breast cancer tissue]. *Pathol.* **1987**, *8*, 138–140.

29. Cakiroglu, E.; Eris, S.; Oz, O.; Karakülah, G.; Senturk, S. Genome-Wide CRISPR Screen Identifies BUB1 Kinase as a Druggable Vulnerability in Malignant Pleural Mesothelioma. *Cell Death Dis.* **2025**, *16*, 241, doi:10.1038/s41419-025-07587-z.

30. Arafeh, R.; Shibue, T.; Dempster, J.M.; Hahn, W.C.; Vazquez, F. The Present and Future of the Cancer Dependency Map. *Nat. Rev. Cancer* **2025**, *25*, 59–73, doi:10.1038/s41568-024-00763-x.

31. Subramanian, A.; Tamayo, P.; Mootha, V.K.; Mukherjee, S.; Ebert, B.L.; Gillette, M.A.; Paulovich, A.; Pomeroy, S.L.; Golub, T.R.; Lander, E.S.; et al. Gene Set Enrichment Analysis: A Knowledge-Based Approach for Interpreting Genome-Wide Expression Profiles. *Proc. Natl. Acad. Sci. U. S. A.* **2005**, *102*, 15545–15550, doi:10.1073/pnas.0506580102.

32. Gingrich, P.W.; Chitsazi, R.; Biswas, A.; Jiang, C.; Zhao, L.; Tym, J.E.; Brammer, K.M.; Li, J.; Shu, Z.; Maxwell, D.S.; et al. canSAR 2024-an Update to the Public Drug Discovery Knowledgebase. *Nucleic Acids Res.* **2025**, *53*, D1287–D1294, doi:10.1093/nar/gkae1050.

33. Kim, E.; Hart, T. Improved Analysis of CRISPR Fitness Screens and Reduced Off-Target Effects with the BAGEL2 Gene Essentiality Classifier. *Genome Med.* **2021**, *13*, 2, doi:10.1186/s13073-020-00809-3.

34. Shen, M.; Kang, Y. Cancer Fitness Genes: Emerging Therapeutic Targets for Metastasis. *Trends Cancer* **2023**, *9*, 69–82, doi:10.1016/j.trecan.2022.08.007.

35. Liu, C.-J.; Hu, F.-F.; Xie, G.-Y.; Miao, Y.-R.; Li, X.-W.; Zeng, Y.; Guo, A.-Y. GSCA: An Integrated Platform for Gene Set Cancer Analysis at Genomic, Pharmacogenomic and Immunogenomic Levels. *Brief. Bioinform.* **2023**, *24*, bbac558, doi:10.1093/bib/bbac558.

36. Hmeljak, J.; Sanchez-Vega, F.; Hoadley, K.A.; Shih, J.; Stewart, C.; Heiman, D.; Tarpey, P.; Danilova, L.; Drill, E.; Gibb, E.A.; et al. Integrative Molecular Characterization of Malignant Pleural Mesothelioma. *Cancer Discov.* **2018**, *8*, 1548–1565, doi:10.1158/2159-8290.CD-18-0804.

37. Chandrashekar, D.S.; Karthikeyan, S.K.; Korla, P.K.; Patel, H.; Shovon, A.R.; Athar, M.; Netto, G.J.; Qin, Z.S.; Kumar, S.; Manne, U.; et al. UALCAN: An Update to the Integrated Cancer Data Analysis Platform. *Neoplasia N. Y. N* **2022**, *25*, 18–27, doi:10.1016/j.neo.2022.01.001.

38. Cheng, X.; Liu, Y.; Wang, J.; Chen, Y.; Robertson, A.G.; Zhang, X.; Jones, S.J.M.; Taubert, S. cSurvival: A Web Resource for Biomarker Interactions in Cancer Outcomes and in Cell Lines. *Brief. Bioinform.* **2022**, *23*, bbac090, doi:10.1093/bib/bbac090.

39. Waldman, T.; Kinzler, K.W.; Vogelstein, B. P21 Is Necessary for the P53-Mediated G1 Arrest in Human Cancer Cells. *Cancer Res.* **1995**, *55*, 5187–5190.

40. Burma, S.; Chen, B.P.; Murphy, M.; Kurimasa, A.; Chen, D.J. ATM Phosphorylates Histone H2AX in Response to DNA Double-Strand Breaks. *J. Biol. Chem.* **2001**, *276*, 42462–42467, doi:10.1074/jbc.C100466200.

41. Møller, P.; Azqueta, A.; Boutet-Robinet, E.; Koppen, G.; Bonassi, S.; Milić, M.; Gajski, G.; Costa, S.; Teixeira, J.P.; Costa Pereira, C.; et al. Minimum Information for Reporting on the Comet Assay (MIRCA): Recommendations for Describing Comet Assay Procedures and Results. *Nat. Protoc.* **2020**, *15*, 3817–3826, doi:10.1038/s41596-020-0398-1.

42. Chaitanya, G.V.; Steven, A.J.; Babu, P.P. PARP-1 Cleavage Fragments: Signatures of Cell-Death Proteases in Neurodegeneration. *Cell Commun. Signal. CCS* **2010**, *8*, 31, doi:10.1186/1478-811X-8-31.

43. Guo, H.; Zhang, X.-Y.; Peng, J.; Huang, Y.; Yang, Y.; Liu, Y.; Guo, X.-X.; Hao, Q.; An, S.; Xu, T.-R. RUVBL1, a Novel C-RAF-Binding Protein, Activates the RAF/MEK/ERK Pathway to Promote Lung Cancer Tumorigenesis. *Biochem. Biophys. Res. Commun.* **2018**, *498*, 932–939, doi:10.1016/j.bbrc.2018.03.084.

44. Lauscher, J.C.; Loddenkemper, C.; Kosel, L.; Gröne, J.; Buhr, H.J.; Huber, O. Increased Pontin Expression in Human Colorectal Cancer Tissue. *Hum. Pathol.* **2007**, *38*, 978–985, doi:10.1016/j.humpath.2007.01.005.

45. Nieto, M.A.; Huang, R.Y.-J.; Jackson, R.A.; Thiery, J.P. EMT: 2016. *Cell* **2016**, *166*, 21–45, doi:10.1016/j.cell.2016.06.028.

46. Taniuchi, K.; Furihata, M.; Iwasaki, S.; Tanaka, K.; Shimizu, T.; Saito, M.; Saibara, T. RUVBL1 Directly Binds Actin Filaments and Induces Formation of Cell Protrusions to Promote Pancreatic Cancer Cell Invasion. *Int. J. Oncol.* **2014**, *44*, 1945–1954, doi:10.3892/ijo.2014.2380.

47. Assimon, V.A.; Tang, Y.; Vargas, J.D.; Lee, G.J.; Wu, Z.Y.; Lou, K.; Yao, B.; Menon, M.-K.; Pios, A.; Perez, K.C.; et al. CB-6644 Is a Selective Inhibitor of the RUVBL1/2 Complex with Anticancer Activity. *ACS Chem. Biol.* **2019**, *14*, 236–244, doi:10.1021/acschembio.8b00904.

48. García-Martín, C.; López-Perrote, A.; Boskovic, J.; Llorca, O. Mechanism of Allosteric Inhibition of RUVBL1-RUVBL2 ATPase by the Small Molecule CB-6644. *Cell Rep. Phys. Sci.* **2024**, *5*, 101982, doi:10.1016/j.xcrp.2024.101982.

49. Hattori, A.; Takamatsu-Ichihara, E.; Yamamoto, Y.; Fujita, S.; Yamagata, K.; Katsumoto, T.; Machida, Y.; Shinohara, H.; Murakami, R.; Kitabayashi, I. Genetic and Chemical Targeting of the ATPase Complex TIP48 and 49 Impairs Acute Myeloid Leukemia. *Leukemia* **2023**, *37*, 1812–1829, doi:10.1038/s41375-023-01971-4.

50. Chernova, T.; Sun, X.M.; Powley, I.R.; Galavotti, S.; Grosso, S.; Murphy, F.A.; Miles, G.J.; Cresswell, L.; Antonov, A.V.; Bennett, J.; et al. Molecular Profiling Reveals Primary Mesothelioma Cell Lines Recapitulate Human Disease. *Cell Death Differ.* **2016**, *23*, 1152–1164, doi:10.1038/cdd.2015.165.

51. Blanquart, C.; Jaurand, M.-C.; Jean, D. The Biology of Malignant Mesothelioma and the Relevance of Preclinical Models. *Front. Oncol.* **2020**, *10*, 388, doi:10.3389/fonc.2020.00388.

52. Robinson, B.W.S.; Creaney, J.; Lake, R.; Nowak, A.; Musk, A.W.; de Klerk, N.; Winzell, P.; Hellstrom, K.E.; Hellstrom, I. Mesothelin-Family Proteins and Diagnosis of Mesothelioma. *Lancet Lond. Engl.* **2003**, *362*, 1612–1616, doi:10.1016/S0140-6736(03)14794-0.

53. Ghanim, B.; Klikovits, T.; Hoda, M.A.; Lang, G.; Szirtes, I.; Setinek, U.; Rozsas, A.; Renyi-Vamos, F.; Laszlo, V.; Grusch, M.; et al. Ki67 Index Is an Independent Prognostic

Factor in Epithelioid but Not in Non-Epithelioid Malignant Pleural Mesothelioma: A Multicenter Study. *Br. J. Cancer* **2015**, *112*, 783–792, doi:10.1038/bjc.2015.9.

54. Gerdes, J.; Lemke, H.; Baisch, H.; Wacker, H.H.; Schwab, U.; Stein, H. Cell Cycle Analysis of a Cell Proliferation-Associated Human Nuclear Antigen Defined by the Monoclonal Antibody Ki-67. *J. Immunol. Baltim. Md 1950* **1984**, *133*, 1710–1715.

55. Richter, M.; Piwocka, O.; Musielak, M.; Piotrowski, I.; Suchorska, W.M.; Trzeciak, T. From Donor to the Lab: A Fascinating Journey of Primary Cell Lines. *Front. Cell Dev. Biol.* **2021**, *9*, 711381, doi:10.3389/fcell.2021.711381.

56. Cree, I.A.; Glaysher, S.; Harvey, A.L. Efficacy of Anti-Cancer Agents in Cell Lines versus Human Primary Tumour Tissue. *Curr. Opin. Pharmacol.* **2010**, *10*, 375–379, doi:10.1016/j.coph.2010.05.001.

57. Zanoni, M.; Piccinini, F.; Arienti, C.; Zamagni, A.; Santi, S.; Polico, R.; Bevilacqua, A.; Tesei, A. 3D Tumor Spheroid Models for in Vitro Therapeutic Screening: A Systematic Approach to Enhance the Biological Relevance of Data Obtained. *Sci. Rep.* **2016**, *6*, 19103, doi:10.1038/srep19103.

58. Baas, P.; Scherpereel, A.; Nowak, A.K.; Fujimoto, N.; Peters, S.; Tsao, A.S.; Mansfield, A.S.; Popat, S.; Jahan, T.; Antonia, S.; et al. First-Line Nivolumab plus Ipilimumab in Unresectable Malignant Pleural Mesothelioma (CheckMate 743): A Multicentre, Randomised, Open-Label, Phase 3 Trial. *Lancet Lond. Engl.* **2021**, *397*, 375–386, doi:10.1016/S0140-6736(20)32714-8.

59. Lorenzini, E.; Torricelli, F.; Zamponi, R.; Donati, B.; Manicardi, V.; Sauta, E.; Faria do Valle, I.; Reggiani, F.; Gugnoni, M.; Manzotti, G.; et al. KAP1 Is a New Non-Genetic Vulnerability of Malignant Pleural Mesothelioma (MPM). *NAR Cancer* **2022**, *4*, zcac024, doi:10.1093/narcan/zcac024.

60. Pandey, G.K.; Landman, N.; Neikes, H.K.; Hulsman, D.; Lieftink, C.; Beijersbergen, R.; Kolluri, K.K.; Janes, S.M.; Vermeulen, M.; Badhai, J.; et al. Genetic Screens Reveal New Targetable Vulnerabilities in BAP1-Deficient Mesothelioma. *Cell Rep. Med.* **2023**, *4*, 100915, doi:10.1016/j.xcrm.2022.100915.

61. Xu, D.; Liang, S.-Q.; Su, M.; Yang, H.; Bruggmann, R.; Oberhaensli, S.; Yang, Z.; Gao, Y.; Marti, T.M.; Wang, W.; et al. Crispr-Mediated Genome Editing Reveals a Preponderance of Non-Oncogene Addictions as Targetable Vulnerabilities in Pleural Mesothelioma. *Lung Cancer Amst. Neth.* **2024**, *197*, 107986, doi:10.1016/j.lungcan.2024.107986.

62. Cakiroglu, E.; Senturk, S. Genomics and Functional Genomics of Malignant Pleural Mesothelioma. *Int. J. Mol. Sci.* **2020**, *21*, 6342, doi:10.3390/ijms21176342.

63. Mao, Y.-Q.; Houry, W.A. The Role of Pontin and Reptin in Cellular Physiology and Cancer Etiology. *Front. Mol. Biosci.* **2017**, *4*, 58, doi:10.3389/fmolb.2017.00058.

64. Gorynia, S.; Bandeiras, T.M.; Pinho, F.G.; McVey, C.E.; Vonrhein, C.; Round, A.; Svergun, D.I.; Donner, P.; Matias, P.M.; Carrondo, M.A. Structural and Functional Insights into a Dodecameric Molecular Machine - the RuvBL1/RuvBL2 Complex. *J. Struct. Biol.* **2011**, *176*, 279–291, doi:10.1016/j.jsb.2011.09.001.

65. Martino, F.; Pal, M.; Muñoz-Hernández, H.; Rodríguez, C.F.; Núñez-Ramírez, R.; Gil-Carton, D.; Degliesposti, G.; Skehel, J.M.; Roe, S.M.; Prodromou, C.; et al. Author Correction: RPAP3 Provides a Flexible Scaffold for Coupling HSP90 to the Human R2TP Co-Chaperone Complex. *Nat. Commun.* **2018**, *9*, 3063, doi:10.1038/s41467-018-05546-1.

66. Gauthier, M.-S.; Cloutier, P.; Coulombe, B. Role of the PAQosome in Regulating Arrangement of Protein Quaternary Structure in Health and Disease. *Adv. Exp. Med. Biol.* **2018**, *1106*, 25–36, doi:10.1007/978-3-030-00737-9_3.

67. Muñoz-Hernández, H.; Pal, M.; Rodríguez, C.F.; Fernandez-Leiro, R.; Prodromou, C.; Pearl, L.H.; Llorca, O. Structural Mechanism for Regulation of the AAA-ATPases RUVBL1-RUVBL2 in the R2TP Co-Chaperone Revealed by Cryo-EM. *Sci. Adv.* **2019**, *5*, eaaw1616, doi:10.1126/sciadv.aaw1616.

68. Izumi, N.; Yamashita, A.; Iwamatsu, A.; Kurata, R.; Nakamura, H.; Saari, B.; Hirano, H.; Anderson, P.; Ohno, S. AAA+ Proteins RUVBL1 and RUVBL2 Coordinate PIKK Activity and Function in Nonsense-Mediated mRNA Decay. *Sci. Signal.* **2010**, *3*, ra27, doi:10.1126/scisignal.2000468.

69. Shin, S.H.; Lee, J.S.; Zhang, J.-M.; Choi, S.; Boskovic, Z.V.; Zhao, R.; Song, M.; Wang, R.; Tian, J.; Lee, M.-H.; et al. Synthetic Lethality by Targeting the RUVBL1/2-TTT Complex in mTORC1-Hyperactive Cancer Cells. *Sci. Adv.* **2020**, *6*, eaay9131, doi:10.1126/sciadv.aay9131.

70. Li, M.; Yang, L.; Chan, A.K.N.; Pokharel, S.P.; Liu, Q.; Mattson, N.; Xu, X.; Chang, W.-H.; Miyashita, K.; Singh, P.; et al. Epigenetic Control of Translation Checkpoint and Tumor Progression via RUVBL1-EEF1A1 Axis. *Adv. Sci. Weinh. Baden-Wurtt. Ger.* **2023**, *10*, e2206584, doi:10.1002/advs.202206584.

71. Vogt, M.; Dudvarski Stankovic, N.; Cruz Garcia, Y.; Hofstetter, J.; Schneider, K.; Kuybu, F.; Hauck, T.; Adhikari, B.; Hamann, A.; Rocca, Y.; et al. Targeting MYC Effector Functions in Pancreatic Cancer by Inhibiting the ATPase RUVBL1/2. *Gut* **2024**, *73*, 1509–1528, doi:10.1136/gutjnl-2023-331519.

72. Cunniff, P.J.; Sivetz, N.; Skopelitis, D.; Klingbeil, O.; Toobian, D.; Maia-Silva, D.; Egeblad, M.; Vakoc, C.R. KLF5 Enables Dichotomous Lineage Programs in Pancreatic Cancer via the AAA+ ATPase Coactivators RUVBL1 and RUVBL2. *Nat. Commun.* **2025**, *16*, 9996, doi:10.1038/s41467-025-66007-0.

73. Chen, J.; Liu, G.; Wu, Y.; Ma, J.; Wu, H.; Xie, Z.; Chen, S.; Yang, Y.; Wang, S.; Shen, P.; et al. CircMYO10 Promotes Osteosarcoma Progression by Regulating miR-370-3p/RUVBL1 Axis to Enhance the Transcriptional Activity of β-Catenin/LEF1 Complex via Effects on Chromatin Remodeling. *Mol. Cancer* **2019**, *18*, 150, doi:10.1186/s12943-019-1076-1.

74. Mangiante, L.; Alcala, N.; Sexton-Oates, A.; Di Genova, A.; Gonzalez-Perez, A.; Khandekar, A.; Bergstrom, E.N.; Kim, J.; Liu, X.; Blazquez-Encinas, R.; et al. Multiomic Analysis of Malignant Pleural Mesothelioma Identifies Molecular Axes and Specialized Tumor Profiles Driving Intertumor Heterogeneity. *Nat. Genet.* **2023**, *55*, 607–618, doi:10.1038/s41588-023-01321-1.

75. Bueno, R.; Stawiski, E.W.; Goldstein, L.D.; Durinck, S.; De Rienzo, A.; Modrusan, Z.; Gnad, F.; Nguyen, T.T.; Jaiswal, B.S.; Chirieac, L.R.; et al. Comprehensive Genomic Analysis of Malignant Pleural Mesothelioma Identifies Recurrent Mutations, Gene Fusions and Splicing Alterations. *Nat. Genet.* **2016**, *48*, 407–416, doi:10.1038/ng.3520.

76. Yi, W.; Dziadowicz, S.A.; Mangano, R.S.; Wang, L.; McBee, J.; Frisch, S.M.; Hazlehurst, L.A.; Adjeroh, D.A.; Hu, G. Molecular Signatures of CB-6644 Inhibition of the RUVBL1/2 Complex in Multiple Myeloma. *Int. J. Mol. Sci.* **2024**, *25*, 9022, doi:10.3390/ijms25169022.

77. Zhang, L.; Mo, J.; Shi, H.; Xiong, J.; Aierken, Y.; Chen, F.; Tang, Y.; Zhao, K.; Lv, Z.; Tan, K. CRISPR-Cas9 Screening Develops an Epigenetic and Transcriptional Gene Signature for Risk Stratification and Target Prediction in Neuroblastoma. *Front. Cell Dev. Biol.* **2024**, *12*, 1433008, doi:10.3389/fcell.2024.1433008.

78. Siaw, J.T.; Claeys, A.; Lai, W.-Y.; Borenäs, M.; Hilgert, E.; Bekaert, S.-L.; Sanders, E.; Kaya, I.; Dorpe, J.V.; Speleman, F.; et al. RUVBL1 and RUVBL2 Are Druggable MYCN Regulators in Neuroblastoma 2024.

79. Sun, F.; Wang, X.; Hu, J.; Liu, J.; Wang, X.; Jia, W.; Yu, Z.; Gao, L.; Dou, B.; Zhao, R.; et al. RUVBL1 Promotes Enzalutamide Resistance of Prostate Tumors through the PLXNA1-CRAF-MAPK Pathway. *Oncogene* **2022**, *41*, 3239–3250, doi:10.1038/s41388-022-02332-8.

80. Chen, D.; Ji, F.; Zhou, Q.; Cheung, H.; Pan, Y.; Lau, H.C.-H.; Liang, C.; Yang, Z.; Huang, P.; Wei, Q.; et al. RUVBL1/2 Blockade Targets YTHDF1 Activity to Suppress m6A-Dependent Oncogenic Translation and Colorectal Tumorigenesis. *Cancer Res.* **2024**, *84*, 2856–2872, doi:10.1158/0008-5472.CAN-23-2081.

81. Tian, J.; Wen, M.; Gao, P.; Feng, M.; Wei, G. RUVBL1 Ubiquitination by DTL Promotes RUVBL1/2-β-Catenin-Mediated Transcriptional Regulation of NHEJ Pathway and Enhances Radiation Resistance in Breast Cancer. *Cell Death Dis.* **2024**, *15*, 259, doi:10.1038/s41419-024-06651-4.

82. Hofstad, M.; Woods, A.; Sychev, Z.E.; Mazzagatti, A.; Huo, X.; Yu, L.; Gilbreath, C.; Chen, W.-M.; Davis, A.J.; Ly, P.; et al. Dual Inhibition of ATR and DNA-PKcs Radiosensitizes ATM-Mutant Prostate Cancer. *Oncogene* **2025**, *44*, 1746–1760, doi:10.1038/s41388-025-03343-x.

83. Srinivasan, G.; Sidhu, G.S.; Williamson, E.A.; Jaiswal, A.S.; Najmunnisa, N.; Wilcoxen, K.; Jones, D.; George, T.J.; Hromas, R. Synthetic Lethality in Malignant Pleural Mesothelioma with PARP1 Inhibition. *Cancer Chemother. Pharmacol.* **2017**, *80*, 861–867, doi:10.1007/s00280-017-3401-y.

84. Yenerall, P.; Das, A.K.; Wang, S.; Kollipara, R.K.; Li, H.; Shan Li, L.; Villalobos, P.; Flaming, J.; Huffman, K.; Timmons, B.C.; et al. A17 Inhibition of RUVBL1/2 ATPase Activity Drives Immune Infiltration and Radiosensitizes Non-Small Cell Lung Cancer. *J. Thorac. Oncol.* **2020**, *15*, S17–S18, doi:10.1016/j.jtho.2019.12.046.

85. Mazzocchi, A.R.; Rajan, S.A.P.; Votanopoulos, K.I.; Hall, A.R.; Skardal, A. In Vitro Patient-Derived 3D Mesothelioma Tumor Organoids Facilitate Patient-Centric Therapeutic Screening. *Sci. Rep.* **2018**, *8*, 2886, doi:10.1038/s41598-018-21200-8.

86. Fang, X.; Shu, L.; Chen, T.; Zhao, X.; Yang, L.; Dou, T.; Yang, L.; Li, X.; Feng, M. Organoids Derived from Patients Provide a New Opportunity for Research and Individualized Treatment of Malignant Peritoneal Mesothelioma. *Mol. Cancer* **2024**, *23*, 12, doi:10.1186/s12943-023-01901-z.

87. Hocking, A.J.; Mortimer, L.A.; Farrall, A.L.; Russell, P.A.; Klebe, S. Establishing Mesothelioma Patient-Derived Organoid Models from Malignant Pleural Effusions. *Lung Cancer Amst. Neth.* **2024**, *191*, 107542, doi:10.1016/j.lungcan.2024.107542.

Figure Legends

Figure 1. Identification of RUVBL1 as a functionally and clinically promising vulnerability in MPM. a Venn diagram showing the overlap of fitness genes identified in H2052 and H2452 cell lines. A total of 85 genes were commonly essential in both models (i). Among these, enzymatic activity (ii) and druggability (iii) filters were applied, resulting in 16 candidate hits. **b** Functional classification of the 85 shared essential genes based on protein class. **c** List of the 25 enzymatic hits, with druggable enzymes highlighted in red and non-druggable ones in black. **d** gRNA scores of RUVBL1 gene for H2052 and H2452 cells. X-axis indicates cell lines and the y-axis represents log2FC (fold change) for each gRNA. **e** and **f** CRISPR gene effect scores (**e**) and expression levels (**f**) of RUVBL1 gene across all MPM cell lines in the DepMap database. The MPM cell lines used in this study are highlighted with red bars. **g** Competitive cell proliferation assay results of H2052 and H2452 cells infected with gRNAs targeting RUVBL1 gene. The percentage of Venus-positive cells at Day 0 was normalized to 100%, and the following measurements were calculated accordingly. Bar graphs are presented as the mean ± SEM of three replicates. **h** Box-Whisker plot of RUVBL1 mRNA expression levels in MPM and normal tissues from GSE42977 and GSE117668 datasets. Statistical significance was calculated by two-tailed Mann-Whitney test. **p<0.01, ***p<0.001. **i** Representative IHC images depicting different immunoreactivity scores (IRS, ranging from 0 to 12) of RUVBL1 staining in MPM tissues. IRS was calculated by the multiplication of proportion of positive cells and the intensity of staining. Scale bar: 100 μm (20X) and 50 μm (40X). **j** IHC-based analysis of RUVBL1 protein expression in human MPM tumor tissues (n = 26) compared to noncancerous normal samples (n = 11). Two-tailed Student's t-test was used for statistical analysis. ***p<0.001. **k** The Kaplan-Meier survival plot

of RUVBL1 in the TCGA MPM dataset compare high gene expression (red) relative to the low/medium or low patients (blue). p-value is shown on the plot.

Figure 2. RUVBL1 is essential for sustaining MPM cell proliferation and maintaining proper cell cycle control. a Western blot assessment of RUVBL1 knockout in H2052 and H2452 cells. Cells were infected with lentiCRISPR v2 gRen (control) or lentiCRISPR v2 RUVBL1 (g1 and g2) lentiviral vectors and selected with puromycin for 3 days. RUVBL1 levels were detected at 9 days post infection. β-actin was used as the equal loading control. **b** BrdU-positive cell percentages are presented as the mean ± SEM, n=6. Two-tailed Student's t-test was used for statistical analysis. **p<0.01, ***p<0.001, ns: not significant. **c** Representative images showing decreased 2D colony formation capacity of H2052 and H2452 cell lines upon RUVBL1 depletion. Colony formation assay was performed in triplicates in 12-well cell culture plates for 10 days. High-resolution images of the plates were acquired by LI-COR Odyssey CLx Imaging System. **d** Crystal violet intensity data showing the relative difference in 2D colony forming capacity of gRen and RUVBL1 gRNA expressing cells. Image Studio software was used to measure signal intensities. Bar graphs are presented as the mean ± SEM of three replicates. Two-tailed Student's t-test was used for statistical analysis. ***p<0.001. **e** Representative images of soft agar colony formation assay. Scale bar: 100 μm. **f** Violin graphs showing the area of colonies. Two-tailed Student's t-test was used for statistical analysis. *p<0.5, ***p<0.001. **g** RUVBL1 protein levels in H2052 and H2452 cells with or without RUVBL1 depletion forced to express gRNA resistant cDNA-encoded wildtype human RUVBL1 protein (mRUVBL1: mutant for gRNA sequence). Cells were infected with pLV-EF1α-Venus-IRES-Puro (Venus) or pLV-EF1α-mRUVBL1-IRES-Puro lentiviral vectors. After 3 days of puromycin selection, cells were infected with high titer of lentiCRISPR v2 gRen (WT) or lentiCRISPR v2 RUVBL1 g2 lentiviral vectors. RUVBL1 levels were detected at 7 days post infection. β-actin served as the equal loading control. **h** Crystal violet intensity data showing the relative difference in 2D colony forming capacity of each group. Image Studio software was used to measure signal intensities. Bar graphs are presented as the mean ± SEM of three replicates. Two-tailed Student's t-test was used for statistical analysis. Asterisks above the bars indicate significance compared to the Venus WT group. *p<0.05, **p<0.01 ***p<0.001. **i** Distribution of cell cycle phases of RUVBL1-depleted cells. Data are presented as mean ± SEM , n=3. **j** p21 protein levels in RUVBL1 WT vs RUVBL1 KO cells. GAPDH was used as a loading control. **k** Representative images of SA-β-Gal staining (blue) assay identifying increased senescence in RUVBL1-depleted cells compared to gRen control cells.

Scale bar: 100 μm. **l** Percentage of SA-β-Gal staining. All cell populations as well as SA-β-Gal stained cells were counted and the percentage of SA-β-Gal staining was calculated by proportioning the number of stained cells to the total number of cells. Data are presented as mean ± SEM, n=8. Two-tailed Student's t-test was used for statistical analysis. ***p<0.001. **m** Gene set enrichment analysis (GSEA) of primary MPM tumor transcriptomes (GSE2549, GSE51024, GSE163722, and GSE29211) showing positive correlations between RUVBL1 expression and hallmark proliferation-associated gene sets, including E2F targets, MYC targets V1, and G2/M checkpoint. Bubble size represents the number of genes per set, and color indicates FDR values.

Figure 3. Disruption of RUVBL1 impairs DNA replication, activates DNA damage signaling, and promotes apoptotic responses. a Representative immunofluorescent staining images of γH2AX expression and localization (Red) in RUVBL1 WT vs RUVBL1 KO cells. DAPI is used for nuclear counterstaining (Blue). Merge images are displayed in the undermost panel. Scale bar: 10 μm **b** The bar graphs summarizing γH2AX total nuclear staining number of RUVBL1 WT vs RUVBL1 KO cells. n=3. Two-tailed Student's t-test was used for statistical analysis. **p<0.01, ***p<0.001. **c** γH2AX protein levels in RUVBL1 WT vs RUVBL1 KO cells. GAPDH was used as a loading control. **d** Representative alkaline comet assay images of RUVBL1 WT and RUVBL1 KO cells. PI staining was observed under fluorescent microscope. **e** The violin graphs represent the distribution of tail length of comets. Comet tail length was calculated by using ImageJ software/OpenComet tool. Two-tailed Student's t-test was used for statistical analysis, n=60. ***p<0.005. **f** ATM and ATR protein levels in RUVBL1 WT vs RUVBL1 KO cells. GAPDH was used as a loading control. **g** Transcriptomic analyses of primary MPM tumors from independent GEO datasets (GSE2549, GSE51024, GSE163722, and GSE29211) showing a negative correlation between RUVBL1 expression and gene sets related to DNA replication and repair pathways. Bubble size indicates the number of genes per set, and color represents FDR values. **h** Bar graphs of the Annexin V/PI apoptosis assay revealing increased apoptosis in RUVBL1-depleted cells compared to gRen control cells. Percentage of apoptotic cells was calculated as the sum of early and late apoptosis. Data are presented as mean ± SEM, n=4 for H2052, n=3 for H2452. Two-tailed Student's t-test was used for statistical analysis. *p<0.05. **i** PARP protein levels in RUVBL1 WT vs RUVBL1 KO cells. GAPDH was used as a loading control.

Figure 4. RUVBL1 depletion impairs MPM cell motility and invasiveness. a Representative images of wound healing in RUVBL1 WT vs RUVBL1 KO cells. Images were taken every 24 hours and representative images were shown from three technical replicates. Scale bar: 100 μm. **b** The graphs represent relative scratch gaps calculated with ImageJ software. Time zero (0) scratch gaps were normalized to 100. Data are presented as mean ± SEM, n=8. Statistical analysis was performed by two-way ANOVA Dunnet's multiple comparisons. ***p<0.001. **c** and **e** Representative images of transwell migration (**c**) and invasion (**e**) assays in RUVBL1-depleted cells, with their relative controls. Scale bar: 100 μm. **d** and **f** Migrated (**d**) and invaded (**f**) number of cells per field. ImageJ software was used for manual cell counting. Data are presented as the mean ± SEM, n=5. Two-tailed Student's t-test was used for statistical analysis. **p<0.01, ***p<0.001.

Figure 5. RUVBL1 promotes EMT and aggressiveness in MPM cells. a RUVBL1 protein levels in empty vector (Venus) and RUVBL1 overexpression vector (RUVBL1) transduced H2052 and H2452 cells. β-actin was used as a loading control. **b** BrdU-positive cell percentages are presented as the mean ± SEM, n=7. Two-tailed Student's t-test was used for statistical analysis. *p<0.05 and ***p<0.001. **c** Representative images of soft agar colony formation assay. Scale bar: 100 μm. **d** Violin graphs showing the area of colonies. Two-tailed Student's t-test was used for statistical analysis. ***p<0.001. **e** Representative immunofluorescent staining images of Phalloidin (green) in RUVBL1 upregulated or control MPM cells. DAPI is used for nuclear counterstaining (Blue). Merge images are displayed in the rightmost panel. The red arrows show Phalloidin localized in cell protrusions. Images were obtained under confocal microscope (magnification 63x), scale bar: 10 μm. **f** The graphs represent relative scratch gaps calculated with ImageJ software. Time zero (0) scratch gaps were normalized to 100. Data are presented as mean ± SEM, n=8. Statistical analysis was performed by two-way ANOVA multiple comparisons. **p<0.01, ***p<0.001. **g** Representative images of transwell invasion assays upon RUVBL1 overexpression with their relative controls. Scale bar: 100 μm. **h** Invaded number of cells per field. ImageJ software was used for manual cell counting. Data are presented as the mean ± SEM, n=5. Two-tailed Student's t-test was used for statistical analysis. ***p<0.001. **i** Relative mRNA expression of epithelial (E-Cad, Ocln) and mesenchymal (N-Cad, Vim) markers in RUVBL1 WT and overexpression clones. mRNA levels were normalized against RPL41 gene using the $2^{-\Delta\Delta Ct}$ method. All the experiments were carried out in triplicate. **j** Vimentin and N-cadherin protein levels in empty vector (Venus) and RUVBL1 overexpression vector (RUVBL1) transduced H2052 cells. β-actin was used as a

loading control. **k** Relative mRNA expression of EMT-associated transcription factors (Snail, Zeb1, Zeb2, Twist1, and Twist2) in RUVBL1 WT and overexpression clones. mRNA levels were normalized against RPL41 gene using the $2^{-\Delta\Delta Ct}$ method. All the experiments were carried out in triplicate. **l** GSEA plots from GSE2549, GSE51024 and GSE163722 datasets. The plots show significantly enriched EMT target gene expression in MPM tumors with high RUVBL1 expression (RUVBL1 High). The y-axis represents the enrichment score (ES). The significance of correlation is depicted on the x-axis, by the red color for positive and the blue color for negative correlation. Normalized enrichment score (NES), false discovery rate (FDR) and p-values are shown.

Figure 6. CB-6644-mediated RUVBL1 inhibition suppresses MPM cell growth and motility while activating DNA damage signaling. a Crystal structure of the human RUVBL1 kinase in complex with CB-6644, as retrieved from CanSar and visualized with PDB (9EMA, https://www.rcsb.org/). red color represents CB-6644. **b** MTT assay measuring the IC50 values of H2052 and H2452. Cells were treated with increasing doses of CB-6644 ranging from 80 nM to 500 nM. Control cells were treated with DMSO. The experiment was performed in 3 technical replicates. **c** BrdU-positive cell percentages are presented as the mean ± SEM, n=8 for H2052 and n=6 for H2452. Two-tailed Student's t-test was used for statistical analysis. ***p<0.001. **d** Representative images showing the impact of pharmacological RUVBL1 inhibition on soft agar colony formation assay. Scale bar: 100 μm. **e** Violin graphs showing the change in the area of colonies upon pharmacological RUVBL1 inhibition. Two-tailed Student's t-test was used for statistical analysis. *p<0.05, ***p<0.001, ns: not significant. **f** Distribution of cell cycle phases of CB-6644 treated H2052 and H2452 cells. Data are presented as mean ± SEM, n=3. **g-j** p21 (**g**), γH2AX (**h**), ATM and ATR (**i**), and PARP (**j**) protein levels in CB-6644 treated cells. GAPDH was used as a loading control. **k** and **m** Representative images of transwell migration (**k**) and invasion (**m**) assays of CB-6644 treated cells, with their relative controls. Scale bar: 100 μm. **l** and **n** Migrated (**l**) and invaded (**n**) number of cells per field. ImageJ software was used for manual cell counting. Data are presented as the mean ± SEM, n=5. Two-tailed Student's t-test was used for statistical analysis. ***p<0.001.

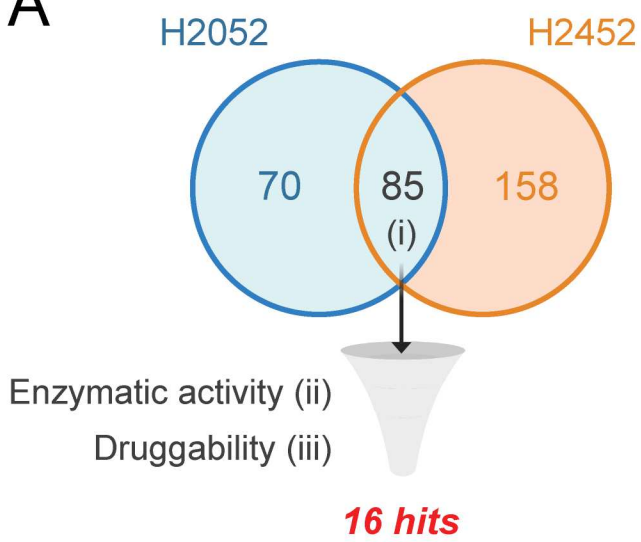
Figure 7. Establishment and Characterization of Patient-Derived Primary MPM Cultures. a Schematic workflow for the establishment of *ex vivo* models, MPM-TPC-D1 and MPM-TPC-D2, from patient-derived tumors. **b** Summary of pathological and clinical characteristics of the source MPM tumors. **c** Representative IHC images depicting hematoxylin

and eosin (H&E), MSLN, Ki-67, and RUVBL1 staining in MPM-TPC-D1 and MPM-TPC-D2 cells. Scale bar: 50 μm (20X) and 20 μm (40X). **d** Representative images showing morphologic features of MPM-TPC-D1 and MPM-TPC-D2 cells. Scale bar: 100 μm. **e** MSLN, Cleaved MSLN, and RUVBL1 protein levels in MPM-TPC-D1 and MPM-TPC-D2 cells. β-actin was used as a loading control. **f** and **g** Representative immunofluorescent staining images of MSLN (red), α-tubulin (green) (**f**) and Ki-67 (red) (**g**) in MPM-TPC-D1 and MPM-TPC-D2 cells. DAPI is used for nuclear counterstaining (Blue). Merge images are displayed in the rightmost panel. Images were obtained under confocal microscope (magnification 63X), scale bar: 10 μm.

Figure 8. RUVBL1 Inhibition Restricts Proliferation, Survival, and Aggressiveness of Primary MPM Cells. a MTT assay measuring the IC50 values of MPM-TPC-D1 and MPM-TPC-D2 cells. Cells were treated with increasing doses of CB-6644 ranging from 0.25 μM to 1.2 μM. Control cells were treated with DMSO. The experiment was performed in 6 technical replicates. **b** Representative images of BrdU incorporation assay showing reduced cell proliferation index (BrdU positivity, green, 12 h labeling) of CB-6644 treated cells. DAPI was used as a nuclear counterstain (Blue). Scale bar: 50 μm. **c** BrdU-positive cell percentages are presented as the mean ± SEM, n=6 for MPM-TPC-D1 and n=9 for MPM-TPC-D2. Two-tailed Student's t-test was used for statistical analysis. **p<0.01, ***p<0.001. **d** Representative images showing 2D colony formation capacity of MPM-TPC-D1 and MPM-TPC-D2 cell lines upon CB-6644 treatment. Experiments were performed in triplicates in 12-well plates. Cells were treated with three different concentrations (0.5×IC50, IC50, and 2×IC50) of CB-6644 and cultured for 10 days. High-resolution images were captured with the LI-COR Odyssey CLx Imaging System. **e** Crystal violet intensity data showing the relative difference in 2D colony forming capacity of Vehicle (DMSO) and CB-6644 treated cells. Image Studio software was used to measure signal intensities. Bar graphs are presented as the mean ± SEMof three replicates. Two-tailed Student's t-test was used for statistical analysis. ***p<0.001. **f** Distribution of cell cycle phases of CB-66442 treated MPM-TPC-D1 and MPM-TPC-D2 cells. **g** PARP protein levels in CB-66442 treated MPM-TPC-D1 and MPM-TPC-D2 cells. β-actin was used as a loading control. **h** Representative images showing the impact of pharmacological RUVBL1 inhibition on spheroid growth. MPM-TPC-D1 and MPM-TPC-D2 cells were grown in 96 well ultra-low attachment plates to form spheroids and treated with CB-6644 for 10 days. Scale bar: 200 μm. **i** Bar graphs showing the decrease in size of spheroids upon pharmacological RUVBL1 inhibition. Data are presented as mean ± SEM, n=3. Two-tailed Student's t-test was used for statistical analysis. *p<0.05, **p<0.01, ***p<0.001. **j** Representative images of

transwell invasion assays of CB-6644 treated cells, with their relative controls. Scale bar: 100 μm. **k** Invaded number of cells per field. ImageJ software was used for manual cell counting. Data are presented as the mean ± SEM, n=6. Two-tailed Student's t-test was used for statistical analysis. **p<0.01, ***p<0.001.

A



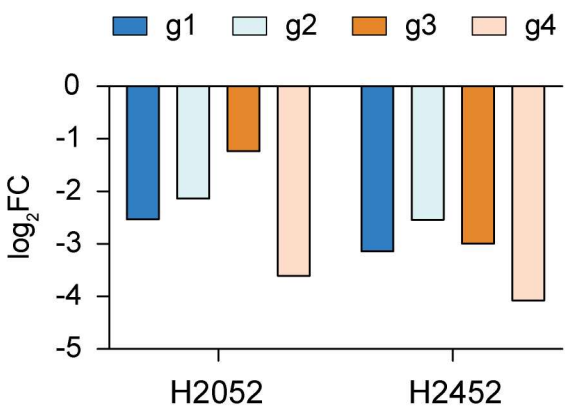
B

Protein Class	#
Enzyme	25
Transporter	5
Metabolic protein	3
Plasma protein	20
Ribosomal protein	14
Other	18
	85

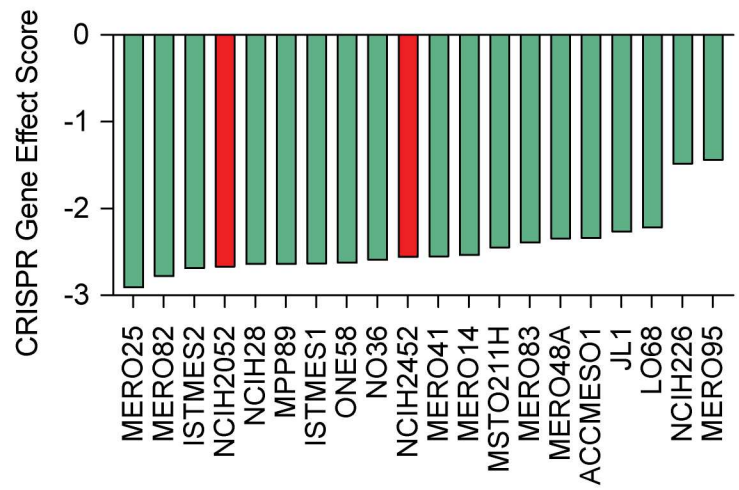
C

Gene Name				
ALG11	IARS	POLR3B	PSMA5	PSMB7
DDX23	MARS	PRIM1	PSMA6	RUVBL1
FNTA	MCM3	PRMT5	PSMA7	TUT1
HMGCS1	MCM7	PSMA2	PSMB3	VARS
HSPA5	NSF	PSMA4	PSMB4	VCP

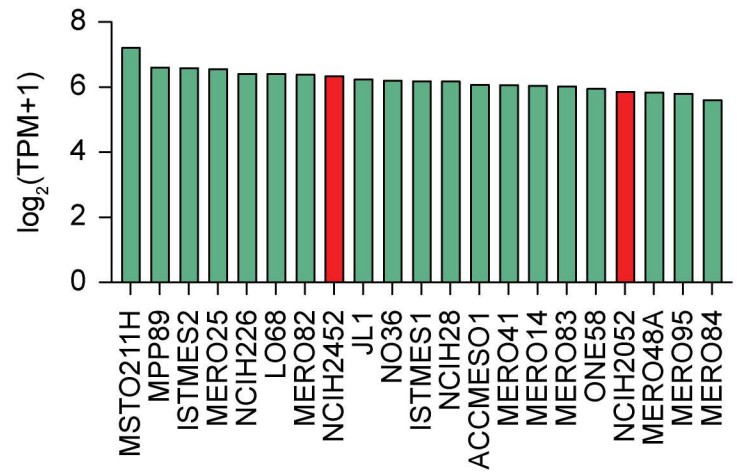
D



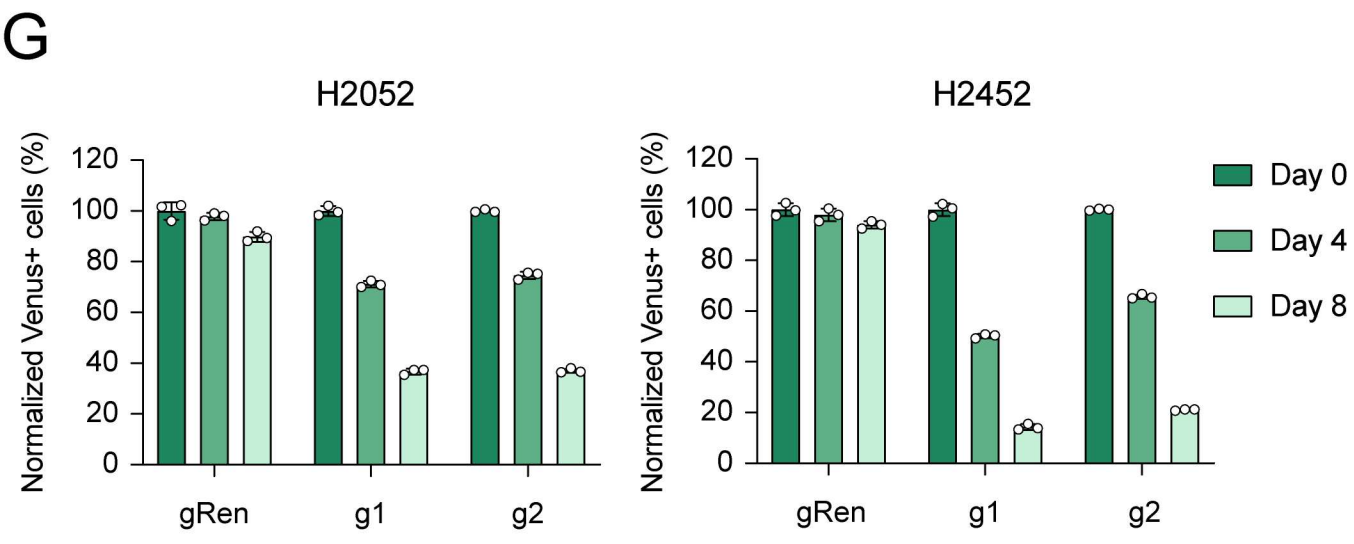
E



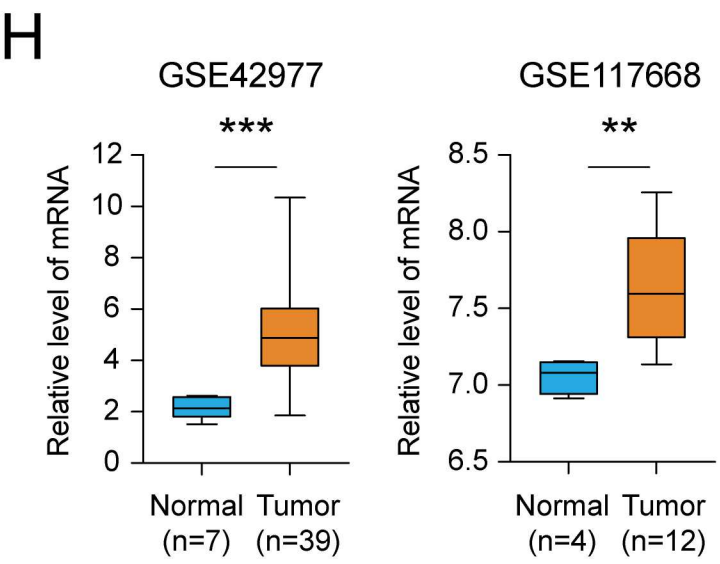
F



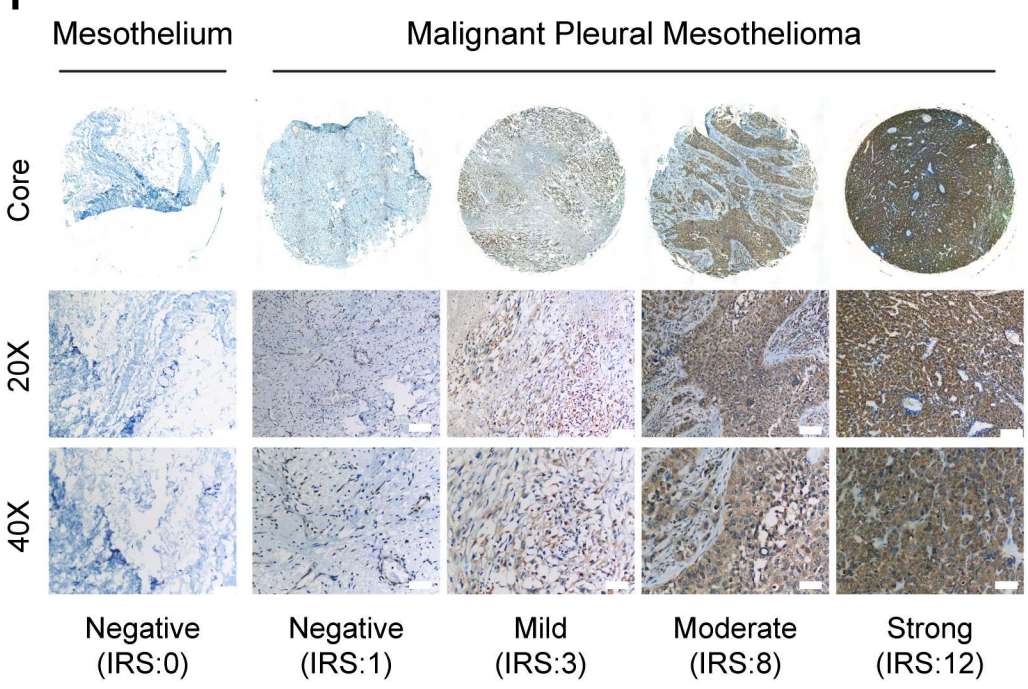
G



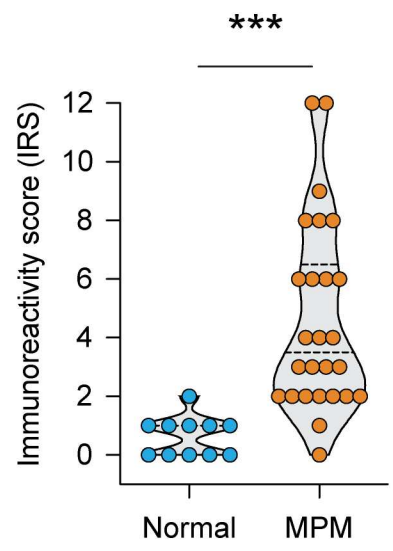
H



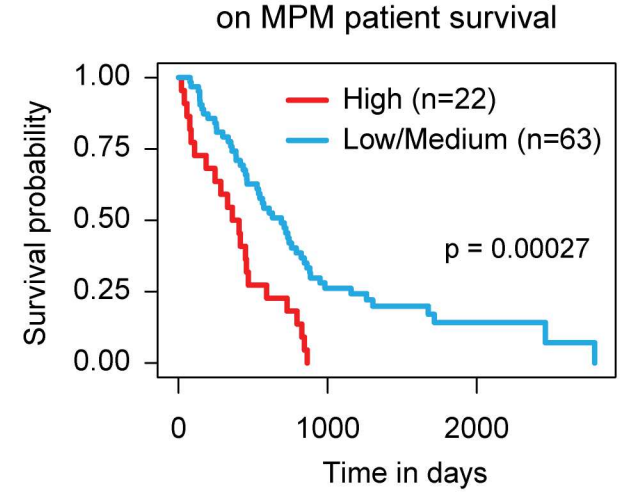
I

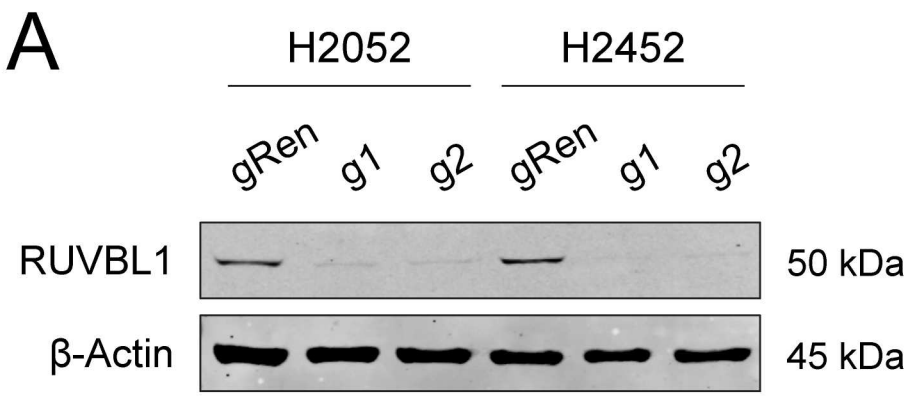


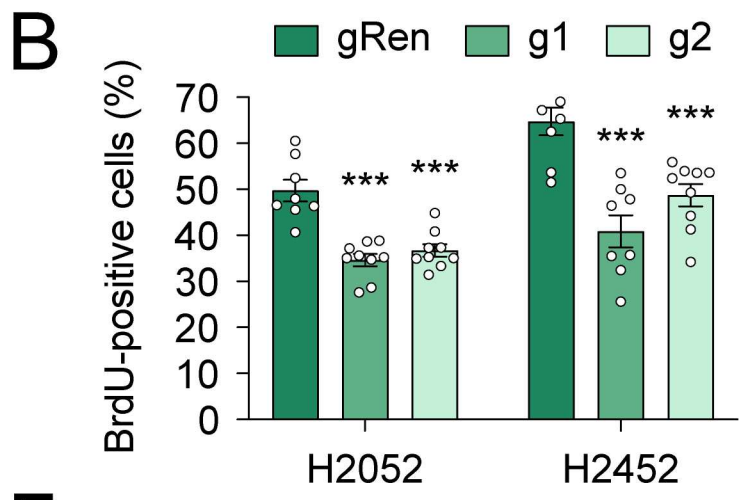
J

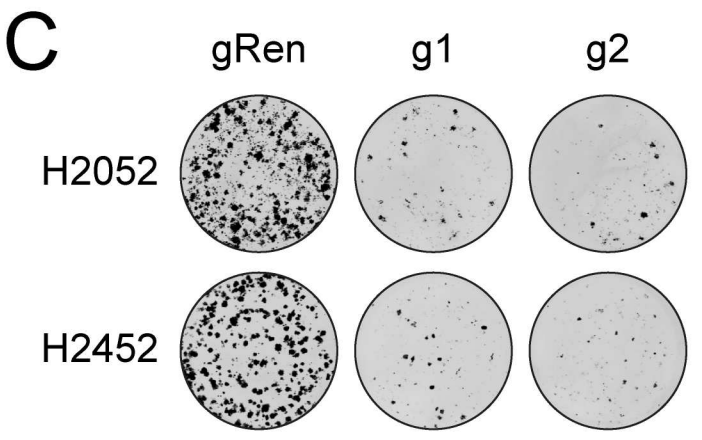


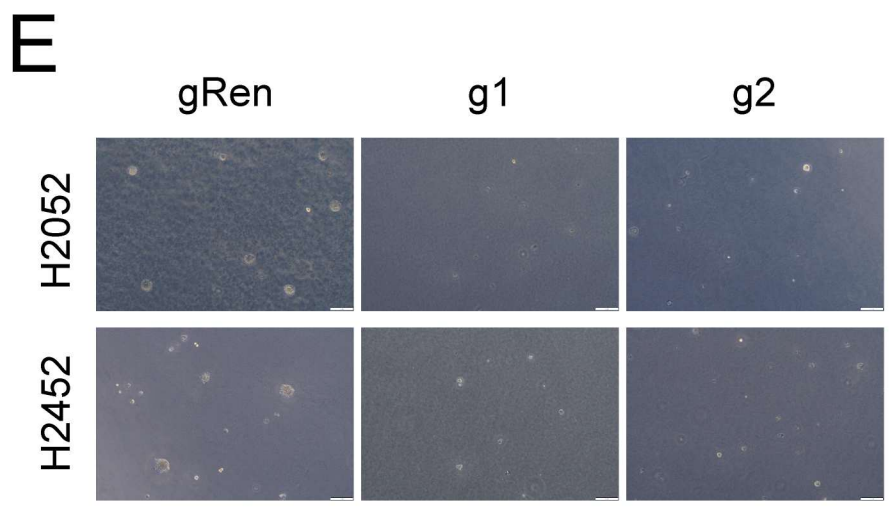
K

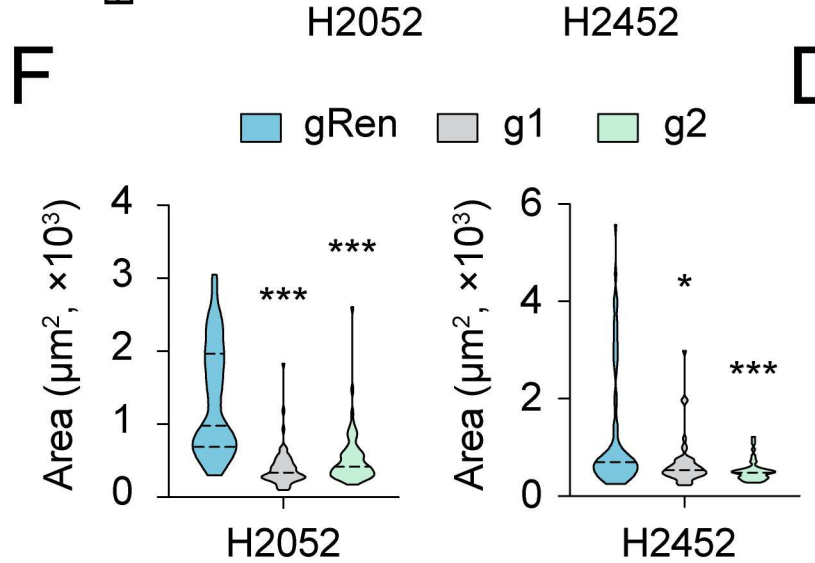


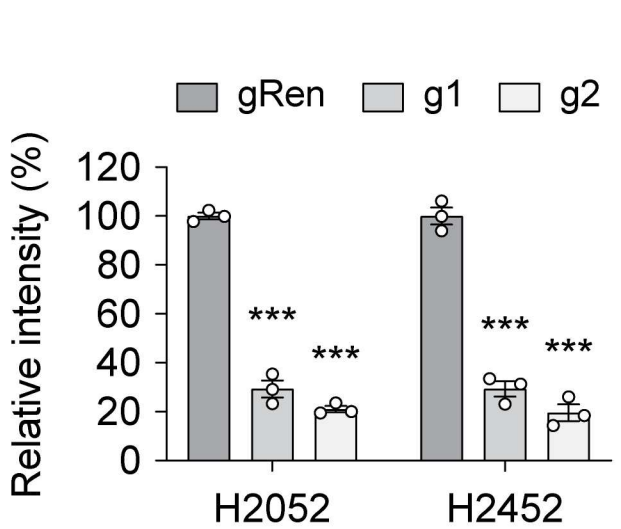


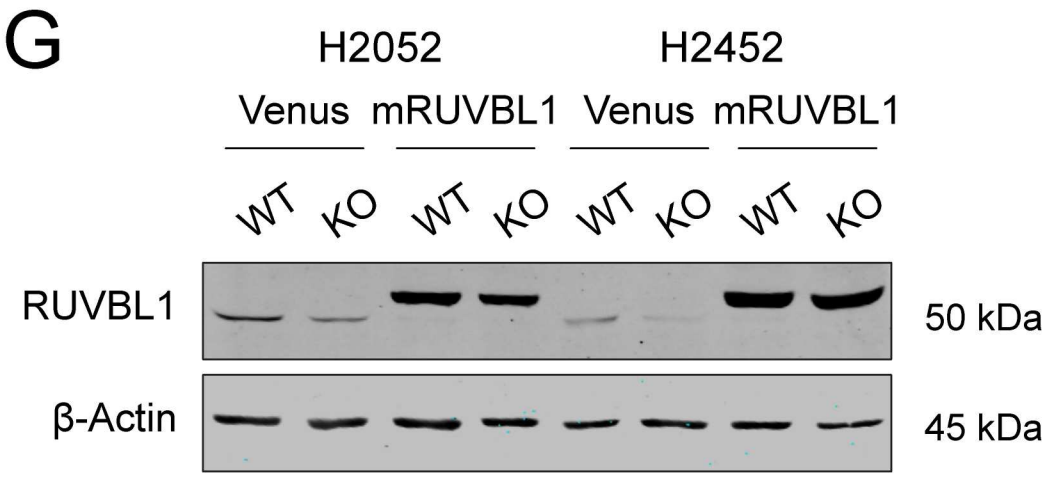


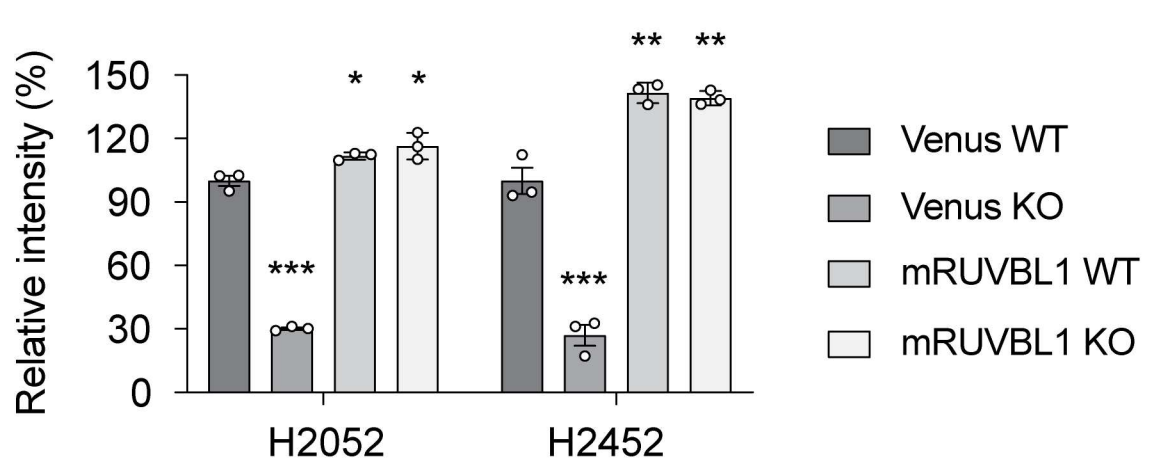


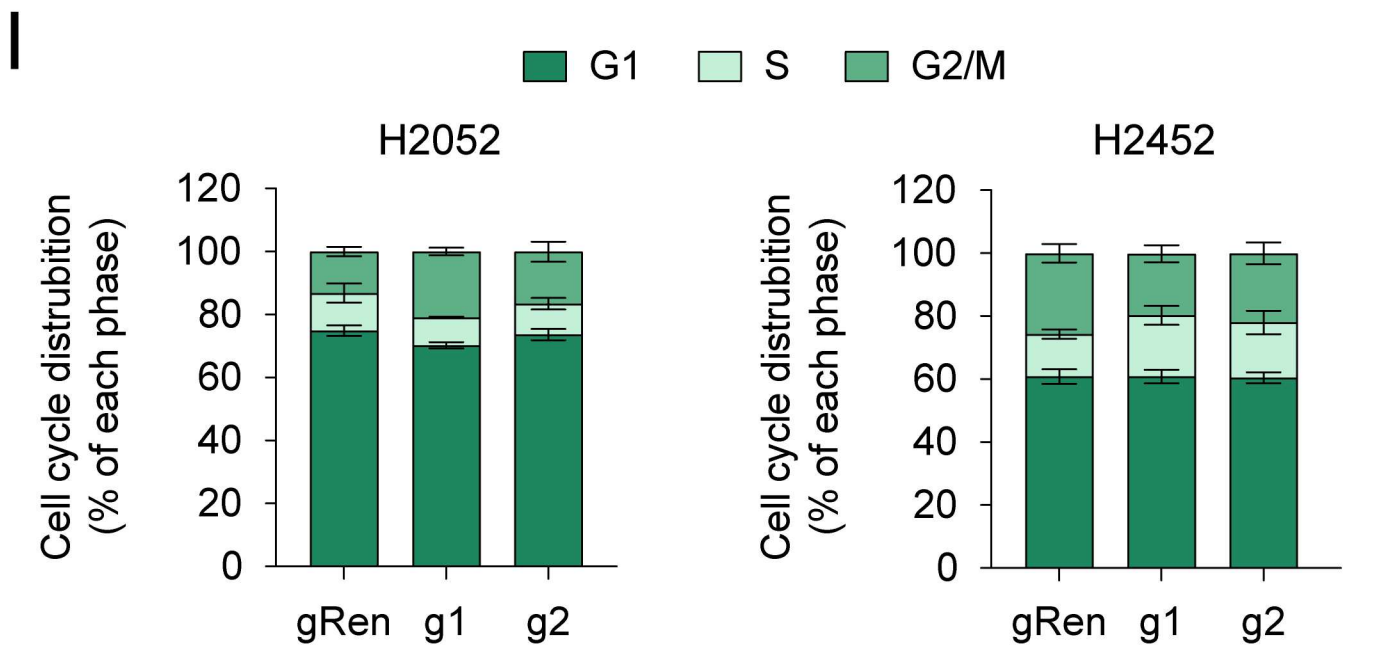






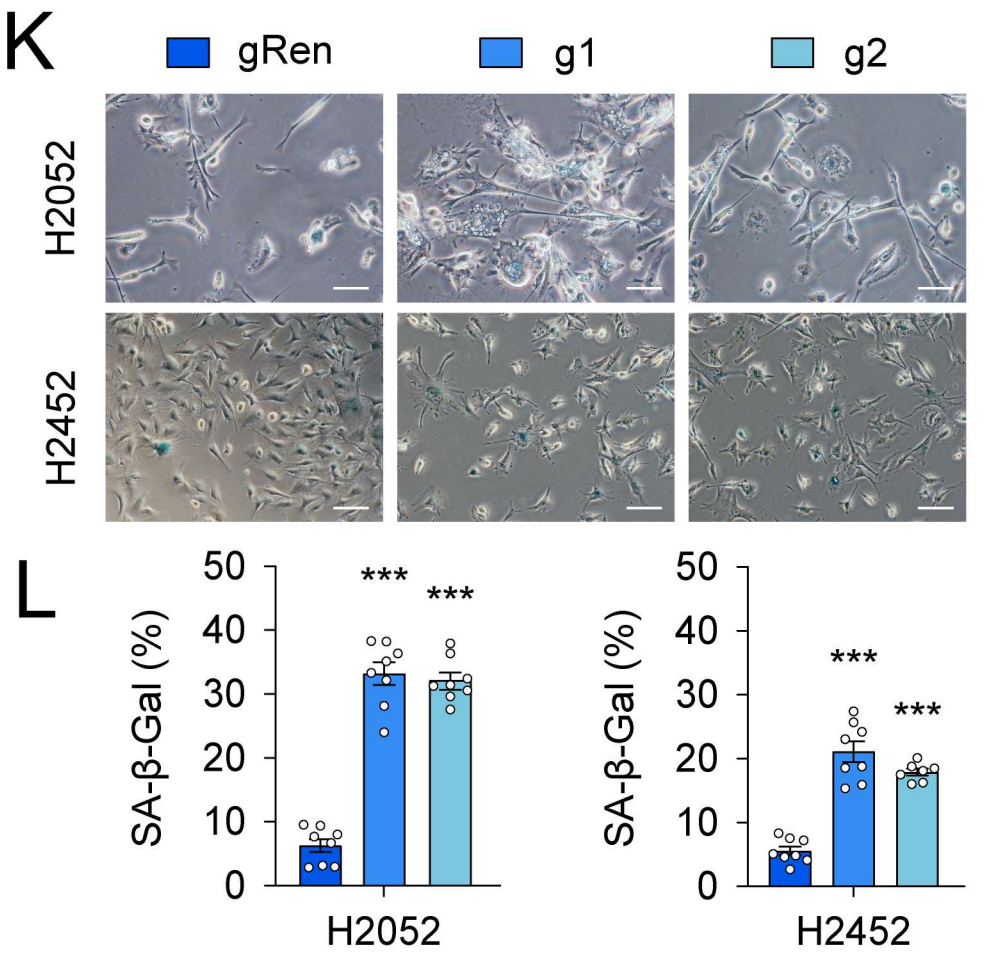


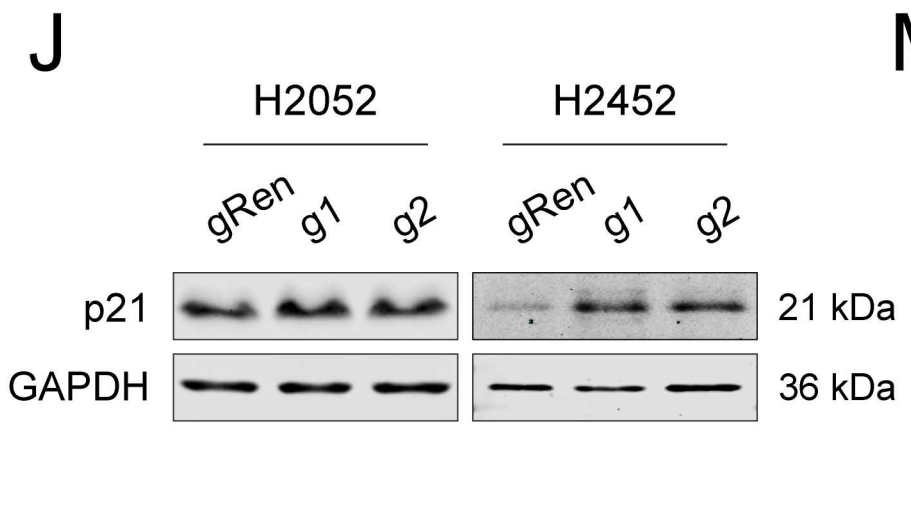


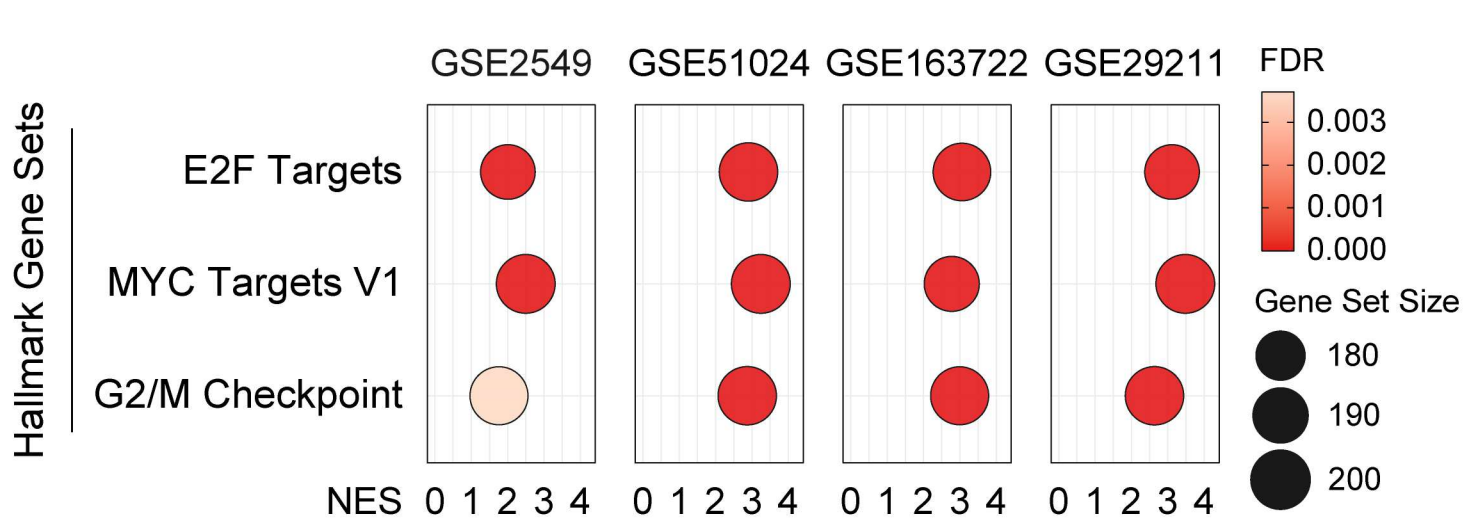


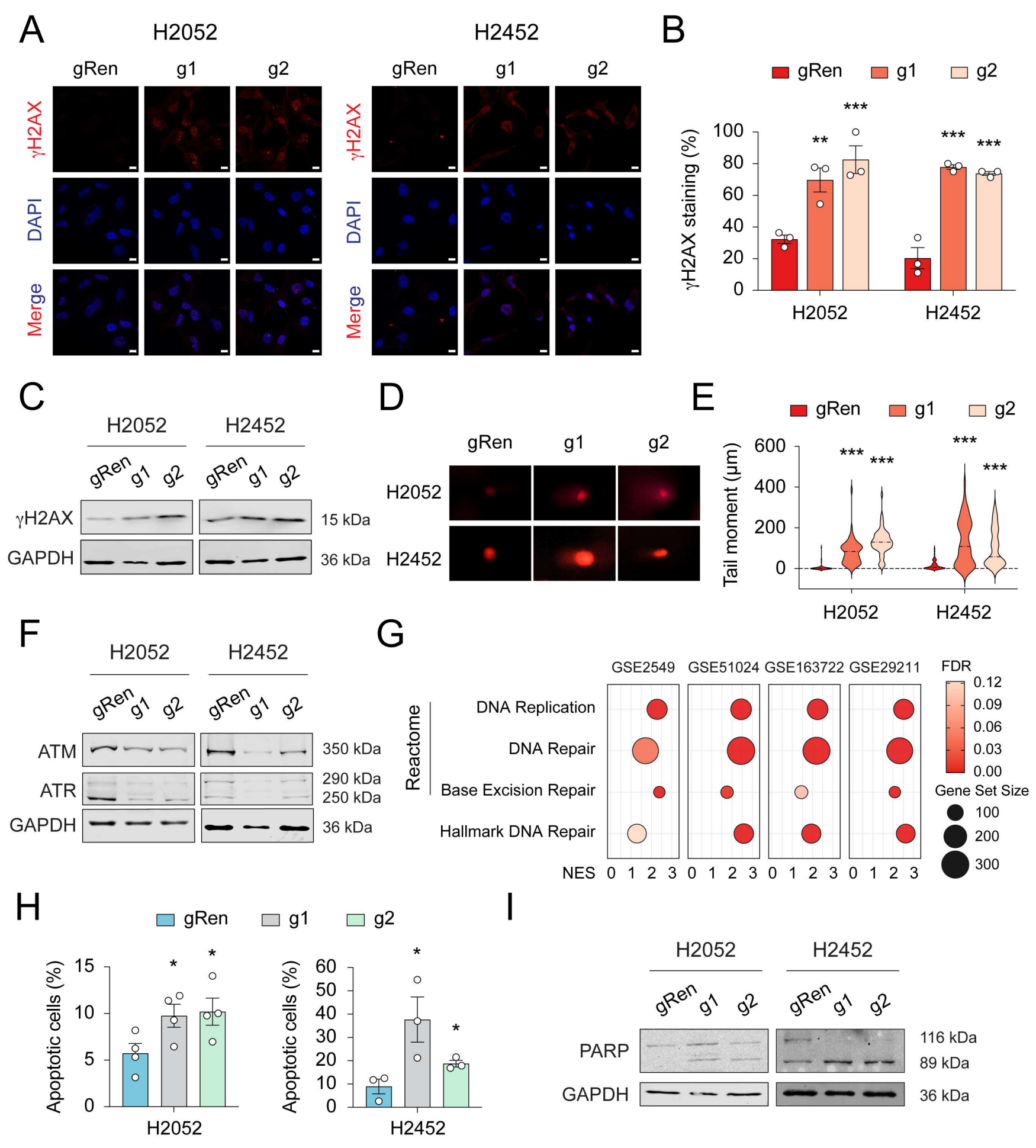
	gRen	g1	g2
G1	74.9±1.7	70.2±1.0	73.7±1.8
S	12.0±3.1	8.8±0.3	9.8±1.8
G2/M	13.2±1.4	20.9±1.2	16.5±3.2

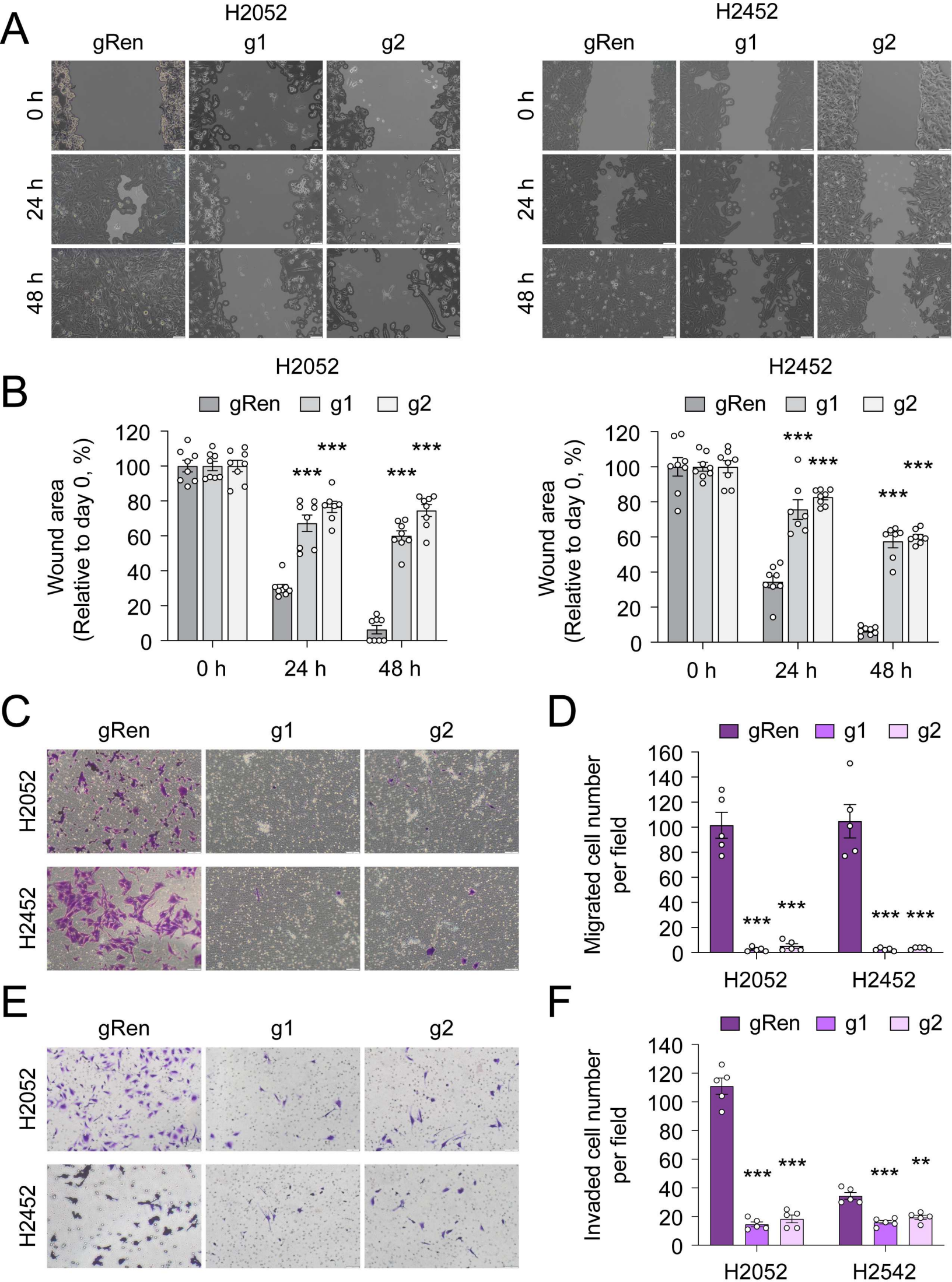
	gRen	g1	g2
G1	60.8±2.3	60.8±2.1	60.4±1.8
S	13.4±1.5	19.4±3.0	17.6±3.7
G2/M	25.7±2.9	19.6±2.7	21.9±3.4

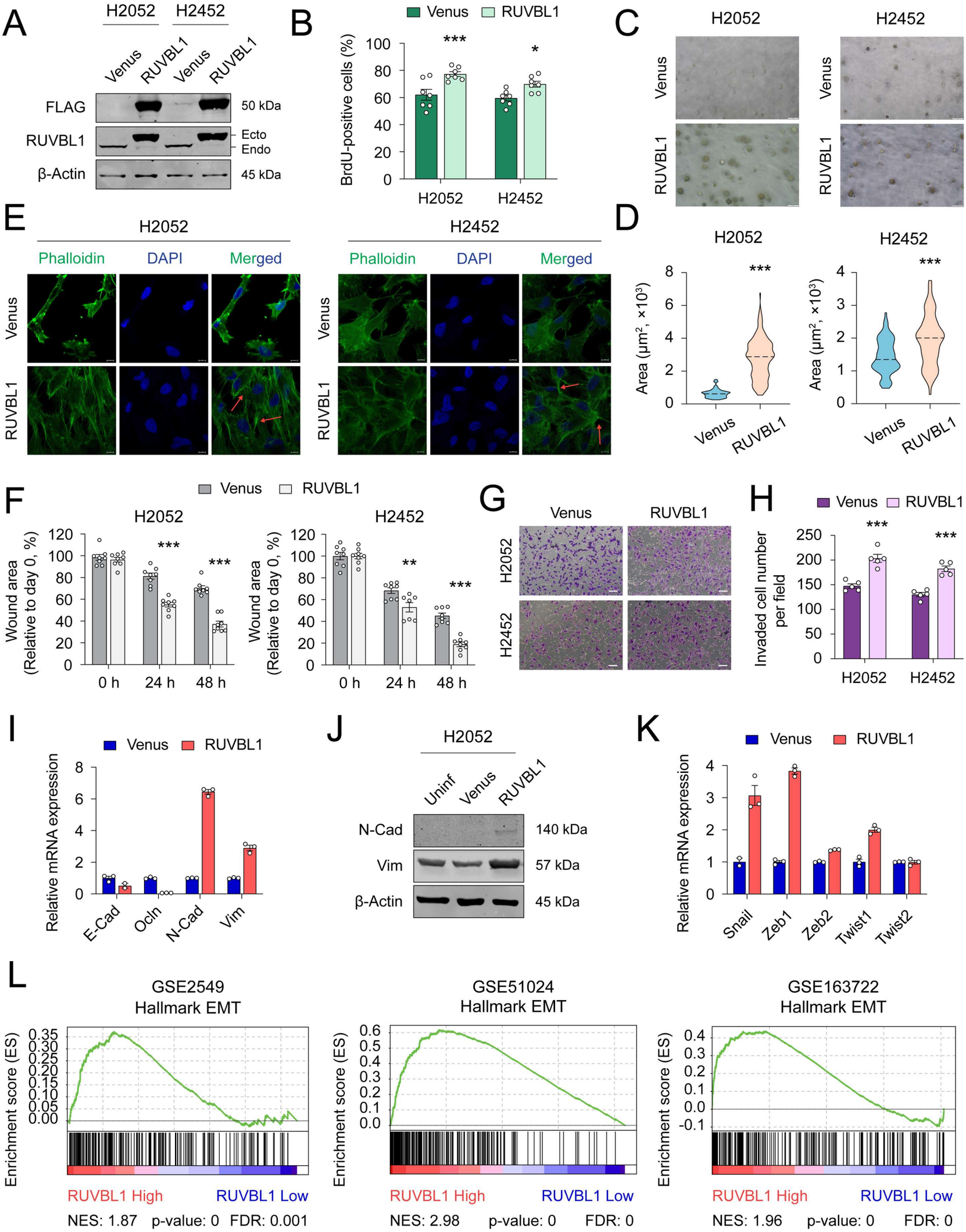


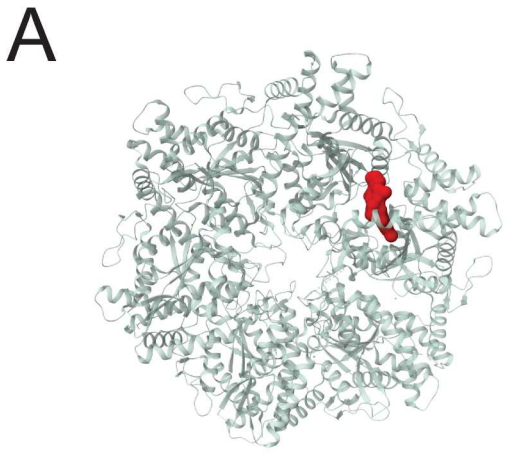


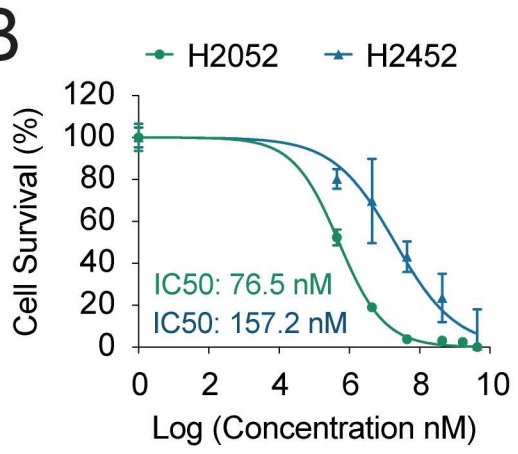


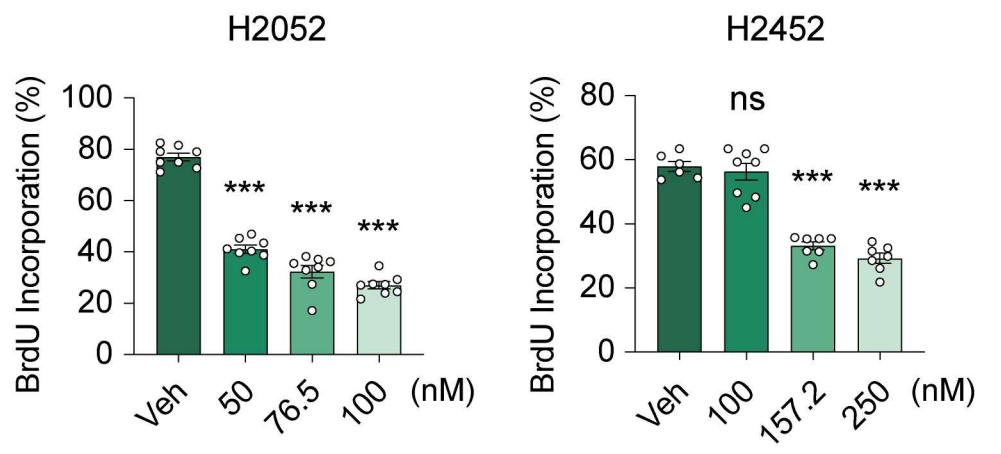

A
H2052
H2452
gRen
g1
g2
γH2AX
DAPI
Merge
B
gRen
g1
g2
γH2AX staining (%)
H2052
H2452
C
H2052
H2452
γH2AX
GAPDH
15 kDa
36 kDa
D
H2052
H2452
E
Tail moment (μm)
H2052
H2452
F
ATM
ATR
GAPDH
350 kDa
290 kDa
250 kDa
36 kDa
G
GSE2549
GSE51024
GSE163722
GSE29211
Reactome
DNA Replication
DNA Repair
Base Excision Repair
Hallmark DNA Repair
NES
FDR
Gene Set Size
H
Apoptotic cells (%)
H2052
H2452
I
PARP
GAPDH
116 kDa
89 kDa
36 kDa

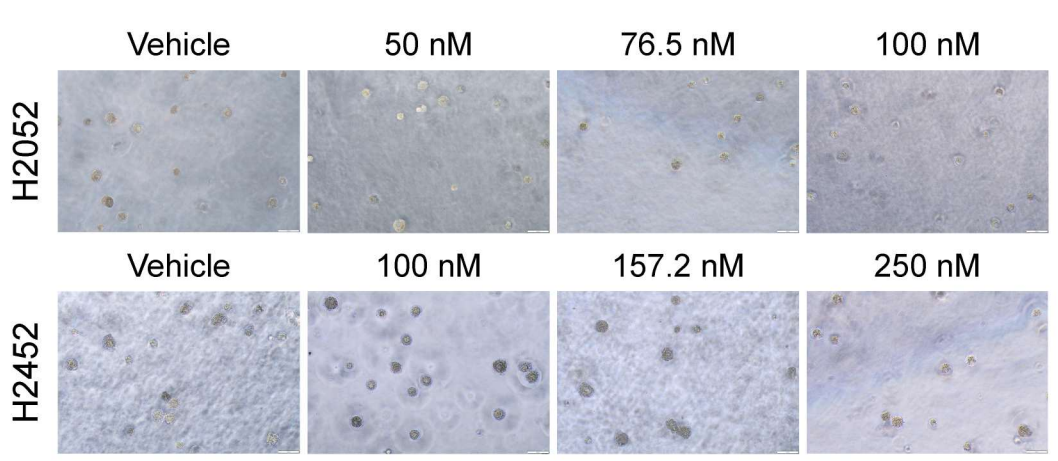

A
H2052
H2452
gRen
g1
g2
0 h
24 h
48 h
B
H2052
H2452
gRen
g1
g2
Wound area
(Relative to day 0, %)
120
100
80
60
40
20
0
***
0 h
24 h
48 h
C
gRen
g1
g2
H2052
H2452
D
gRen
g1
g2
Migrated cell number
per field
160
140
120
100
80
60
40
20
0
***
H2052
H2452
E
gRen
g1
g2
H2052
H2452
F
gRen
g1
g2
Invaded cell number
per field
140
120
100
80
60
40
20
0
***
**
H2052
H2542

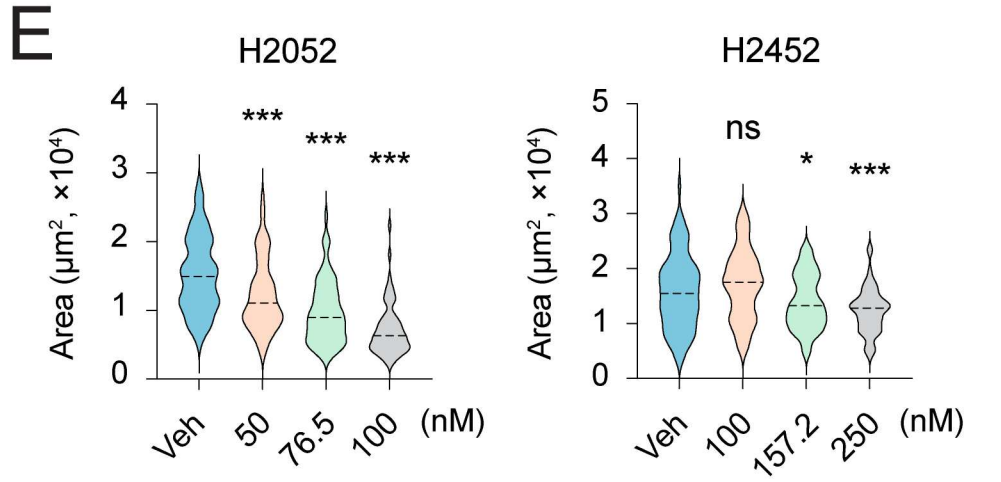

A
H2052
H2452
Venus
RUVBL1
Venus
RUVBL1
FLAG
RUVBL1
β-Actin
50 kDa
Ecto
Endo
45 kDa
B
Venus
RUVBL1
BrdU-positive cells (%)
***
*
H2052
H2452
C
H2052
H2452
Venus
RUVBL1
D
H2052
H2452
***
Area (μm², ×10³)
Venus
RUVBL1
E
H2052
H2452
Phalloidin
DAPI
Merged
Venus
RUVBL1
F
Venus
RUVBL1
H2052
H2452
Wound area (Relative to day 0, %)
***
**
0 h
24 h
48 h
G
Venus
RUVBL1
H2052
H2452
H
Venus
RUVBL1
Invaded cell number per field
***
H2052
H2452
I
Venus
RUVBL1
Relative mRNA expression
E-Cad
Ocln
N-Cad
Vim
J
H2052
Uninf
Venus
RUVBL1
N-Cad
Vim
β-Actin
140 kDa
57 kDa
45 kDa
K
Venus
RUVBL1
Relative mRNA expression
Snail
Zeb1
Zeb2
Twist1
Twist2
L
GSE2549
Hallmark EMT
GSE51024
Hallmark EMT
GSE163722
Hallmark EMT
Enrichment score (ES)
RUVBL1 High
RUVBL1 Low
NES: 1.87 p-value: 0 FDR: 0.001
NES: 2.98 p-value: 0 FDR: 0
NES: 1.96 p-value: 0 FDR: 0

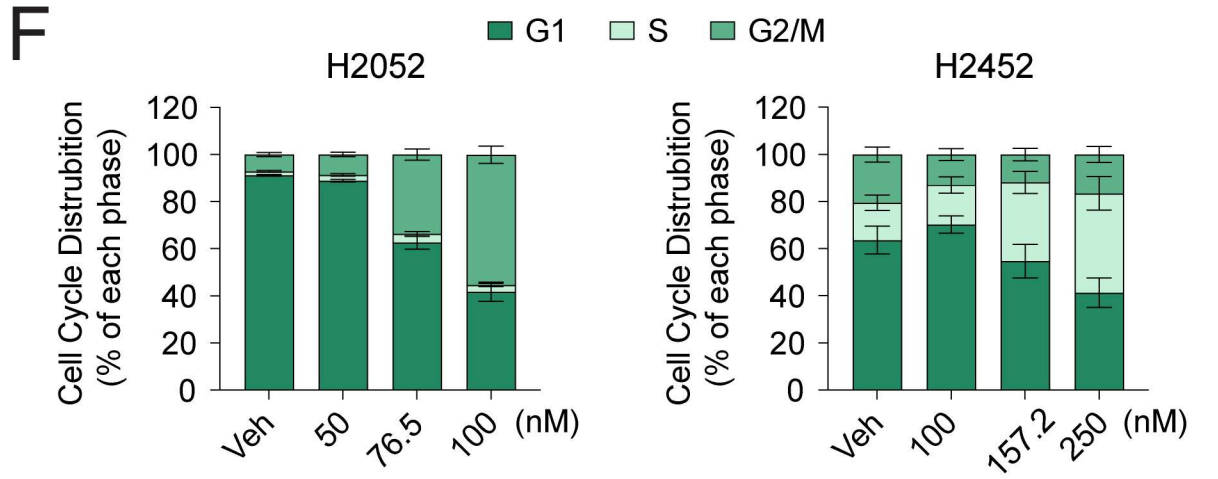






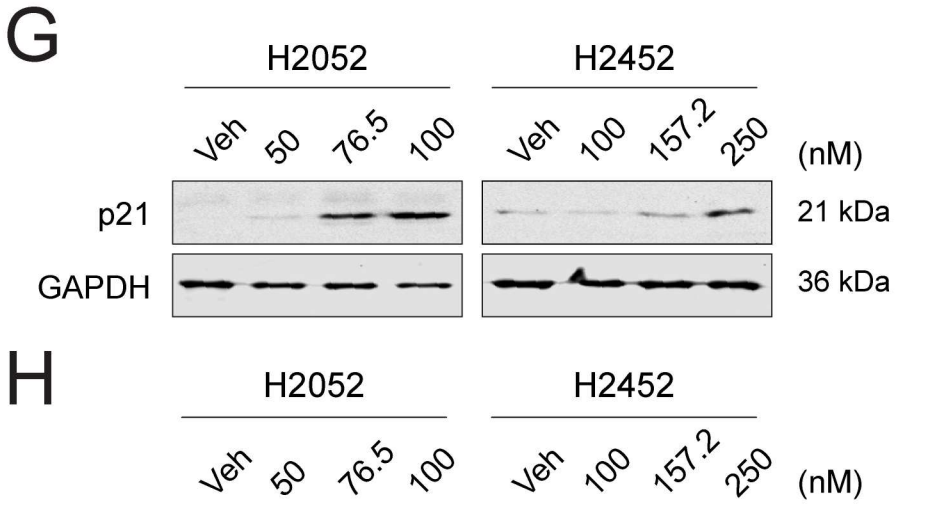


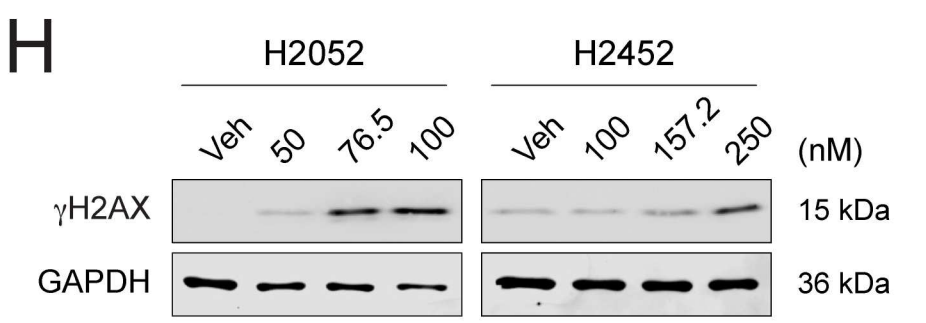


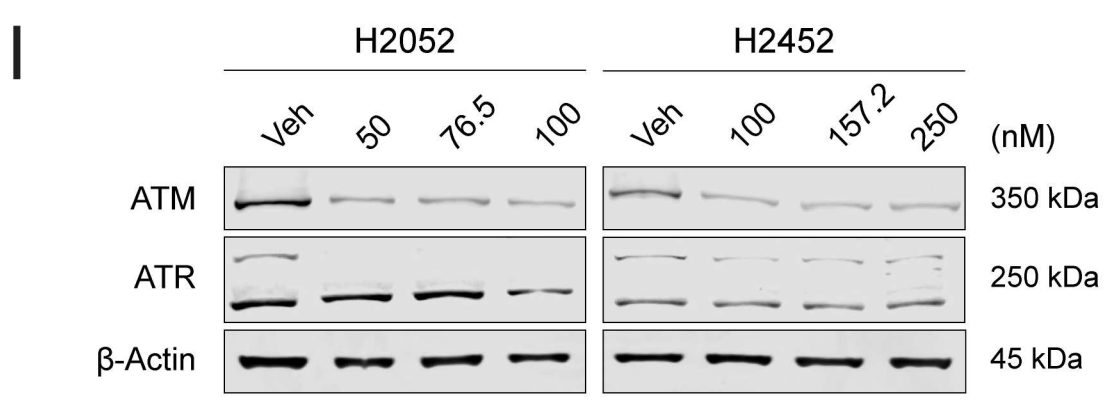


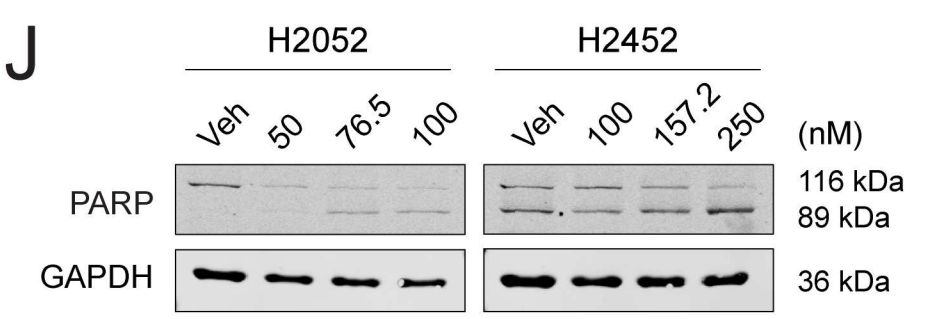
(nM)	Veh	50	76.5	100
G1	91.1±0.4	88.9±0.6	62.6±2.8	41.7±4.1
S	1.7±0.5	2.4±0.5	3.7±1.0	2.9±0.7
G2/M	7.2±0.8	8.7±0.9	33.7±2.4	55.2±3.7

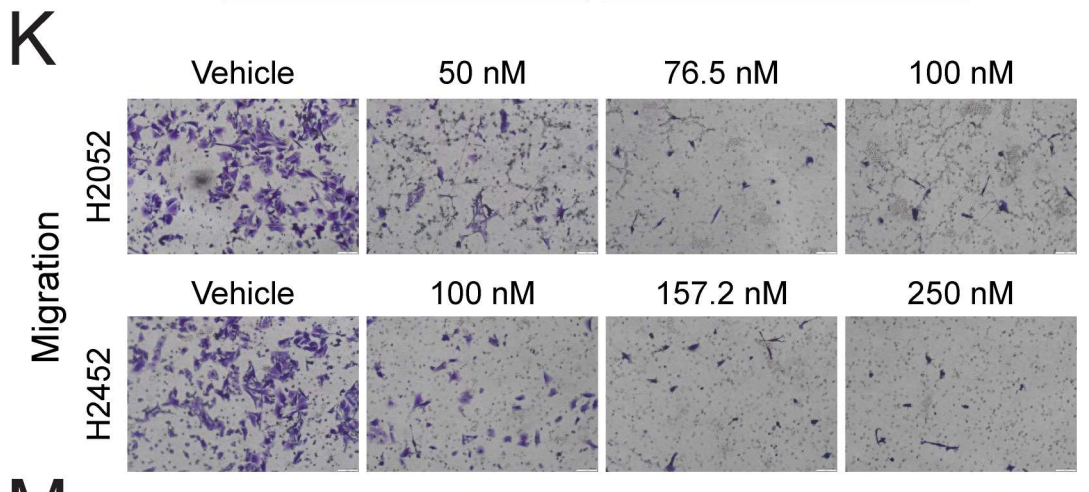
(nM)	Veh	100	157.2	250
G1	63.7±5.9	70.2±3.6	54.7±7.1	41.4±6.3
S	15.8±3.3	16.8±3.5	33.4±4.7	42.1±7.1
G2/M	20.5±3.2	13.0±2.6	11.9±2.6	16.5±3.4

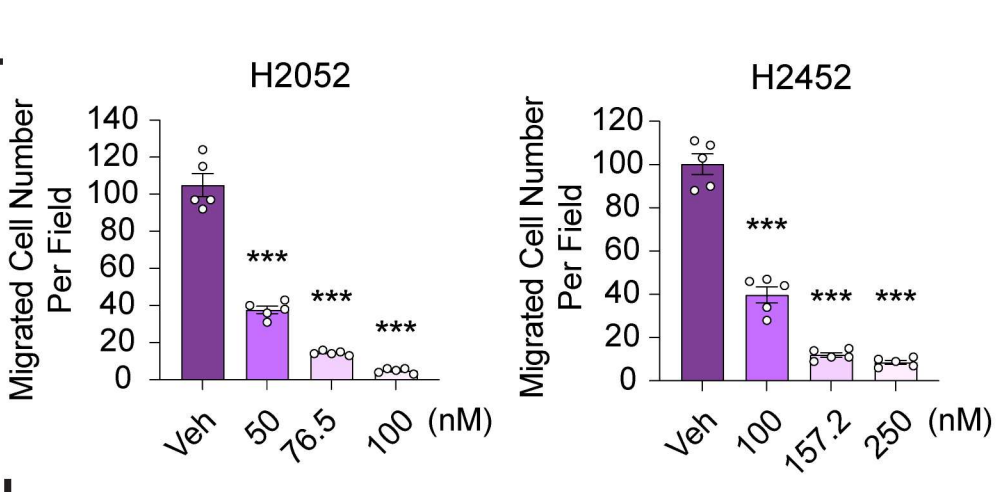


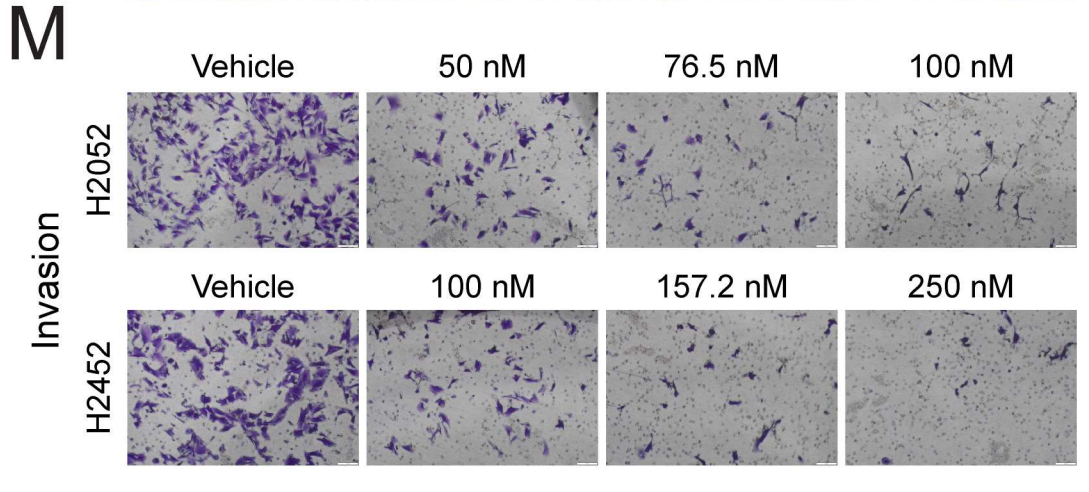


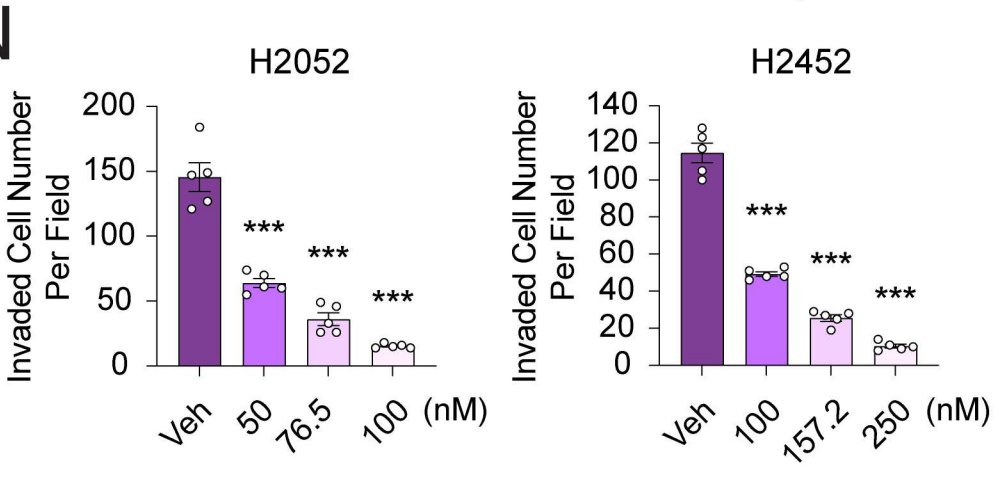




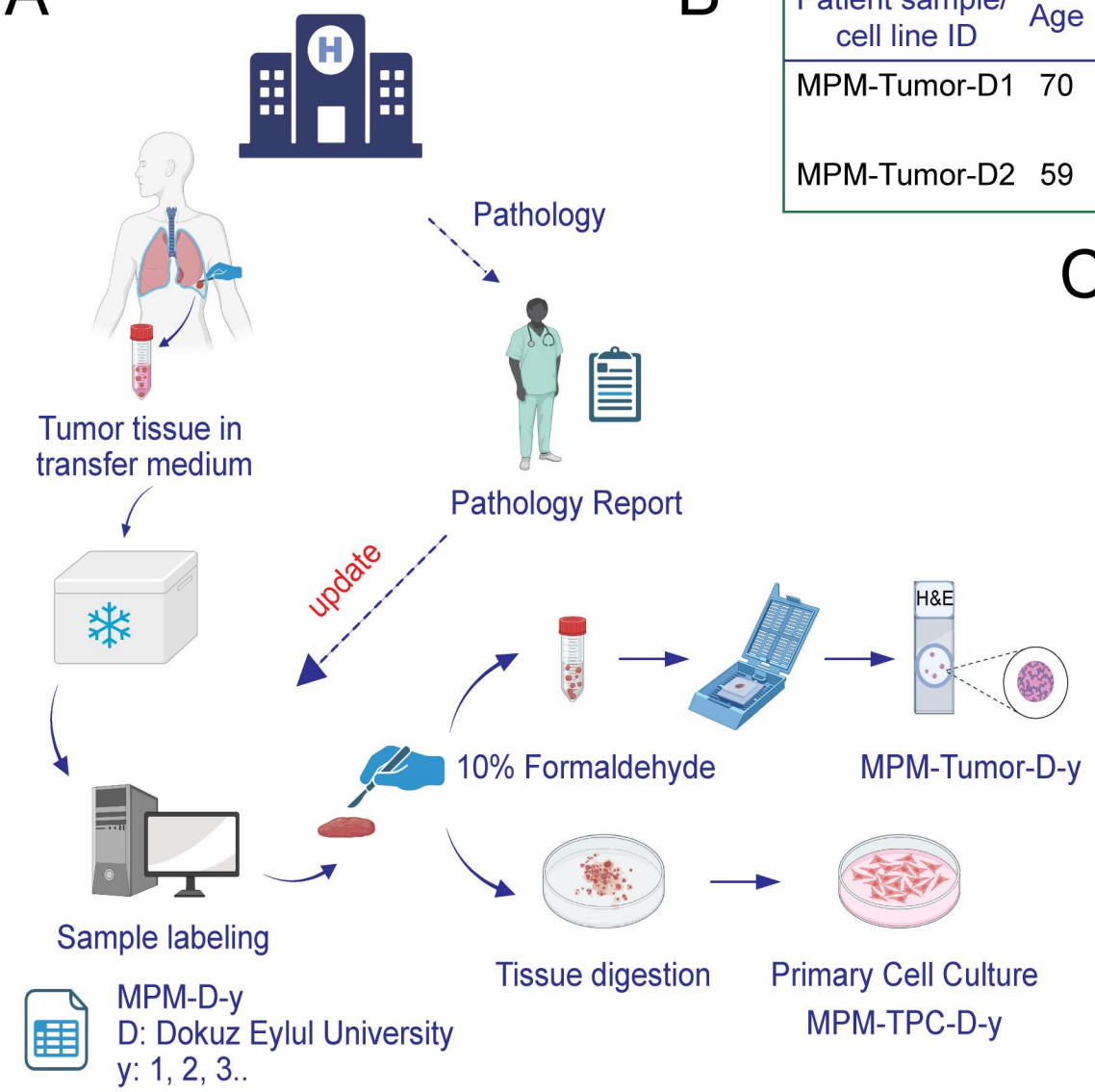








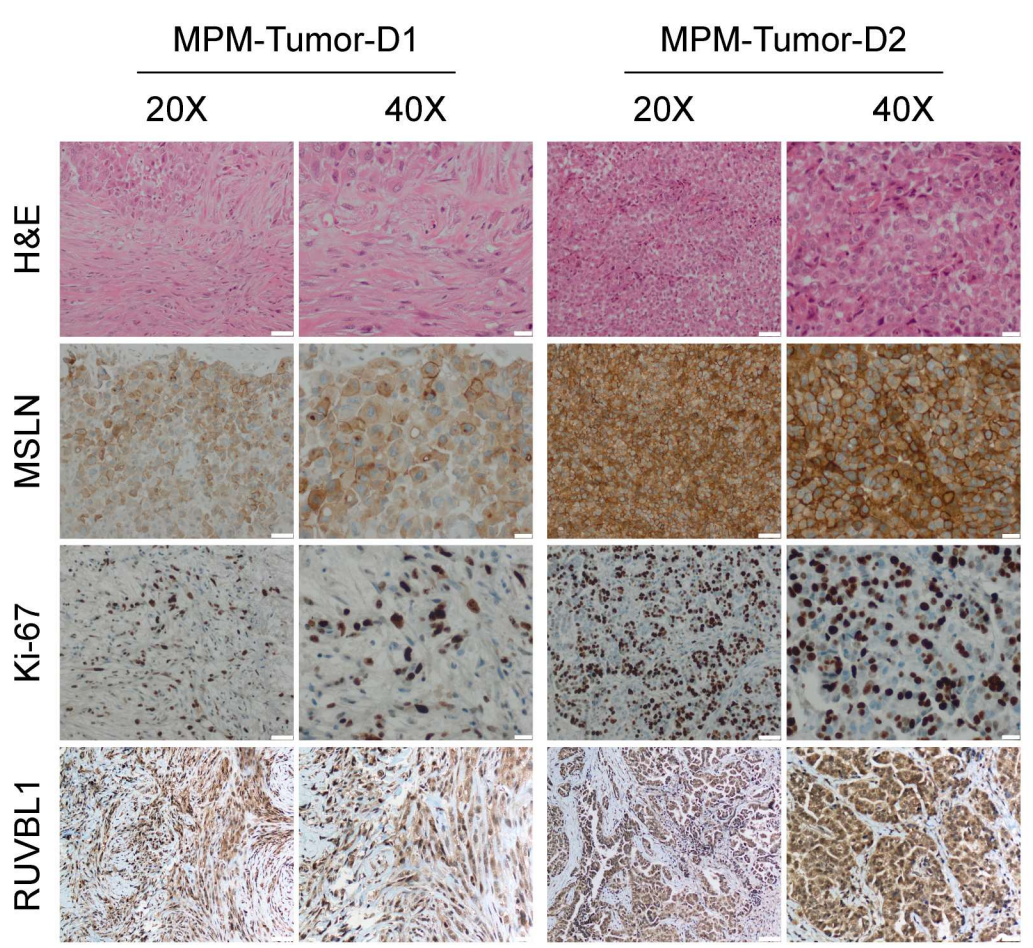
A



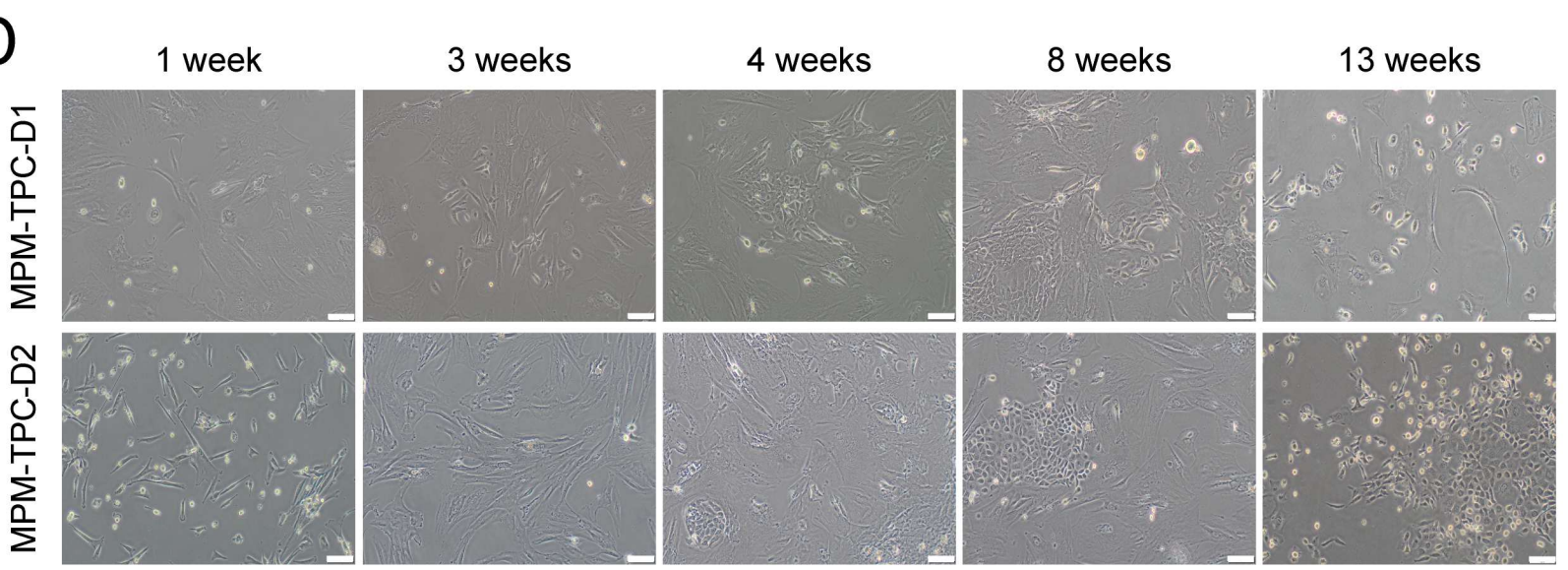
B

Patient sample/ cell line ID	Age	Sex	Asbestos exposure	Histopathology	Clinical diagnosis
MPM-Tumor-D1	70	Male	Yes	Biphasic	Calretinin (+), D240 (-), BER-EP4 (-), WT-1 (+), HBME-1 (+)
MPM-Tumor-D2	59	Female	Yes	Epithelioid	Calretinin (+), BER-EP4 (-)

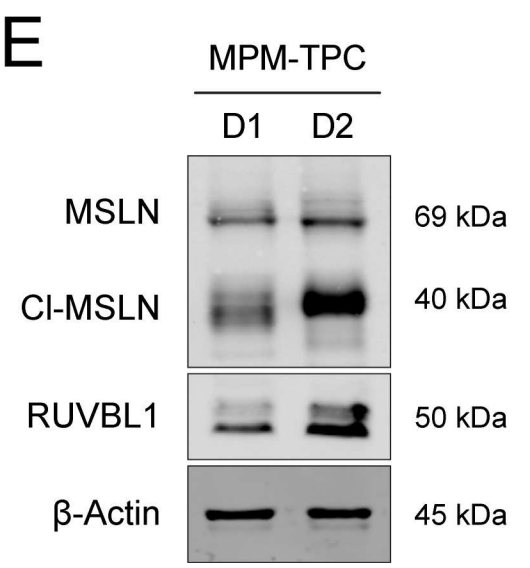
C



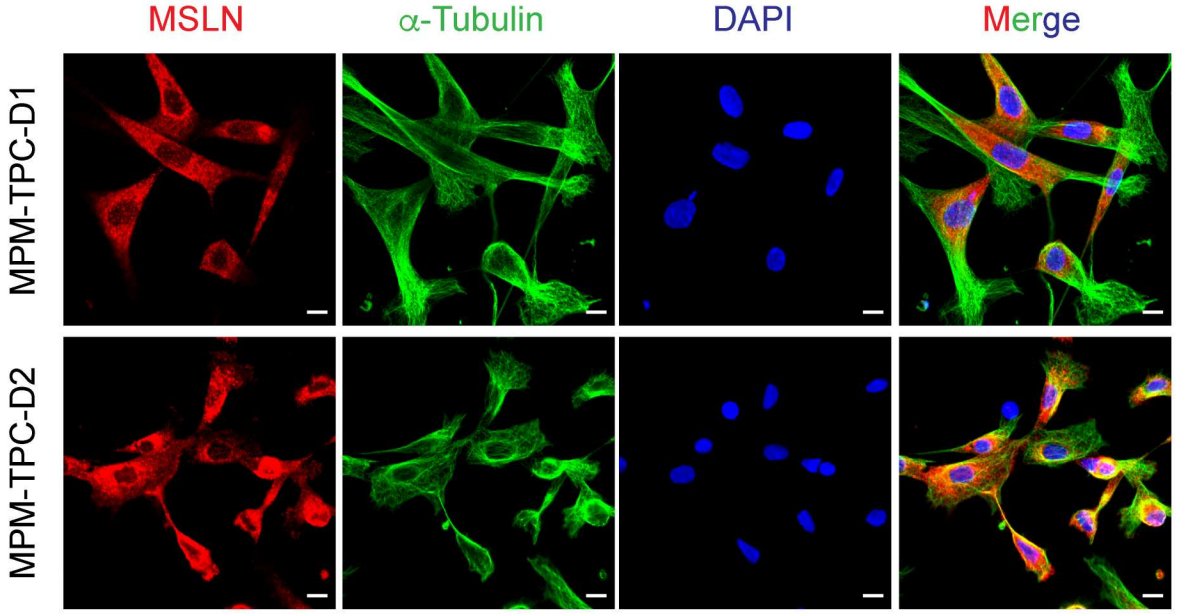
D



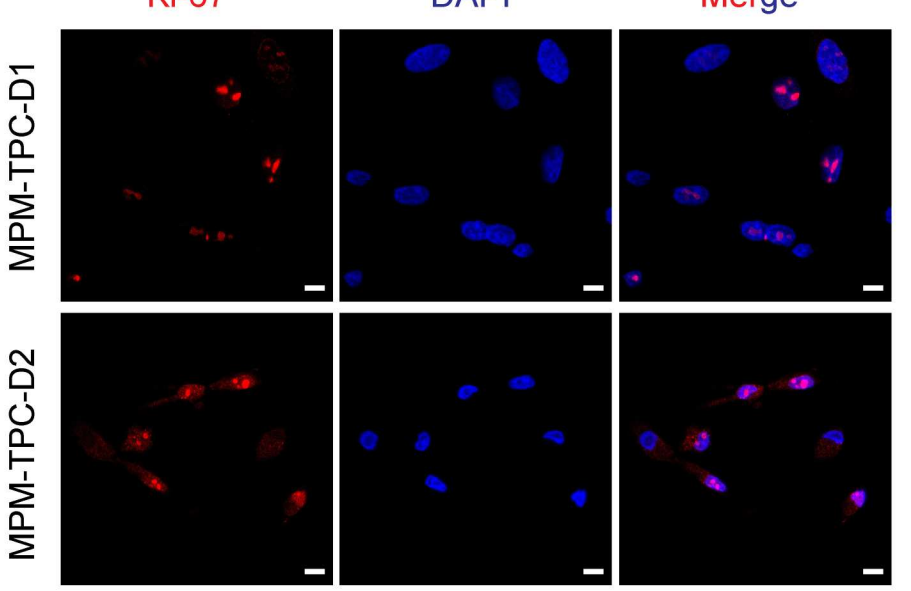
E



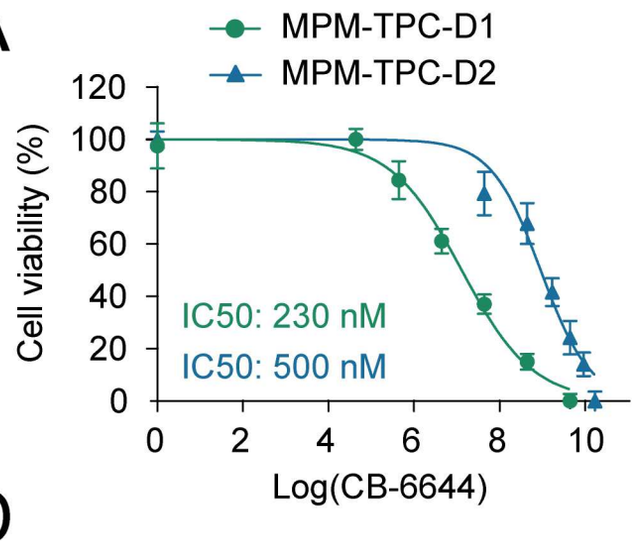
F



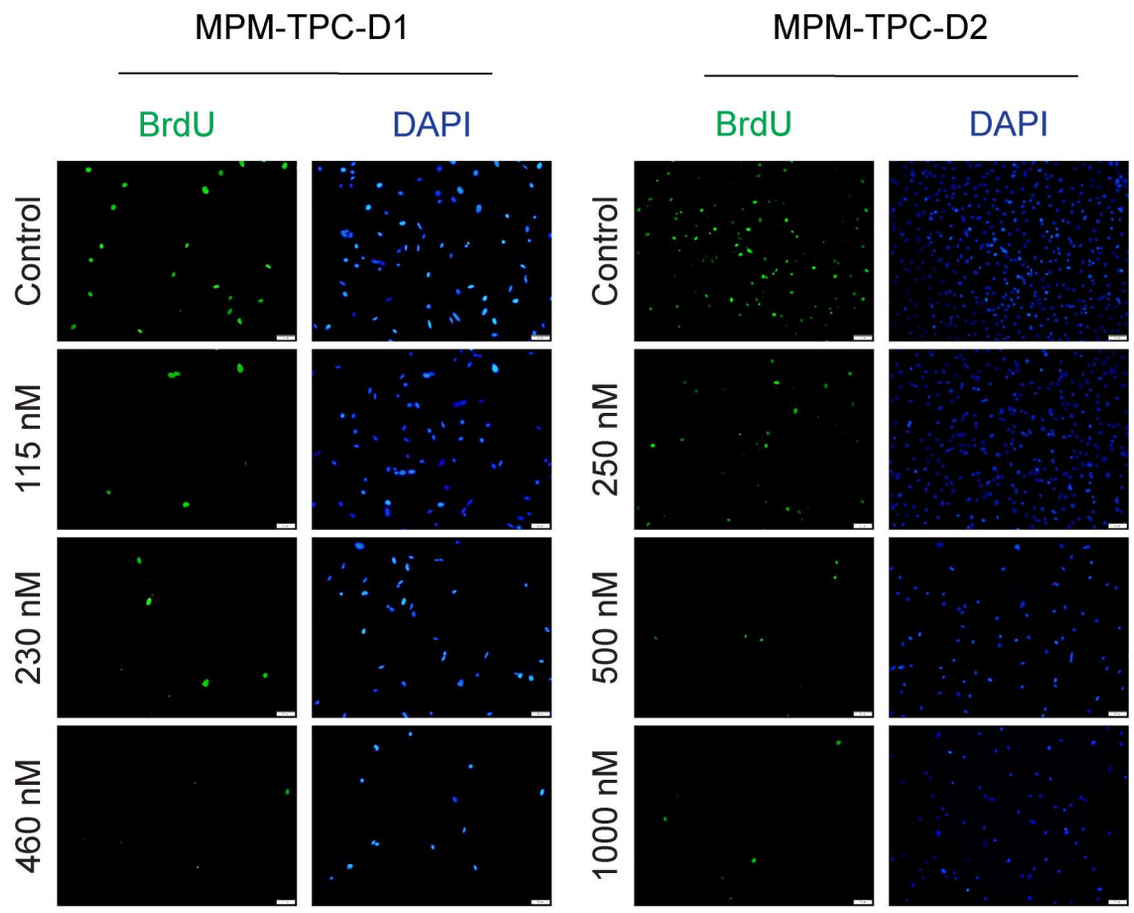
G



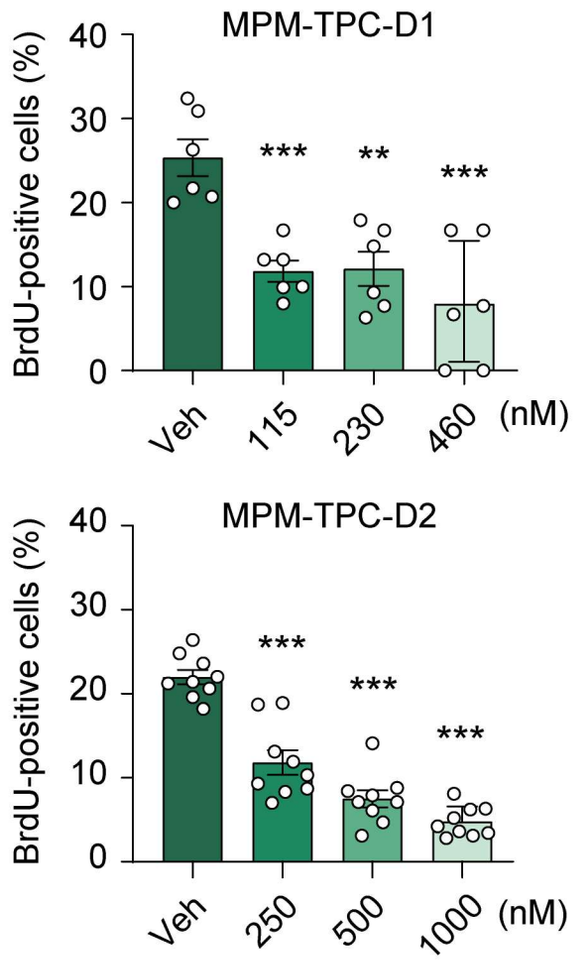
A



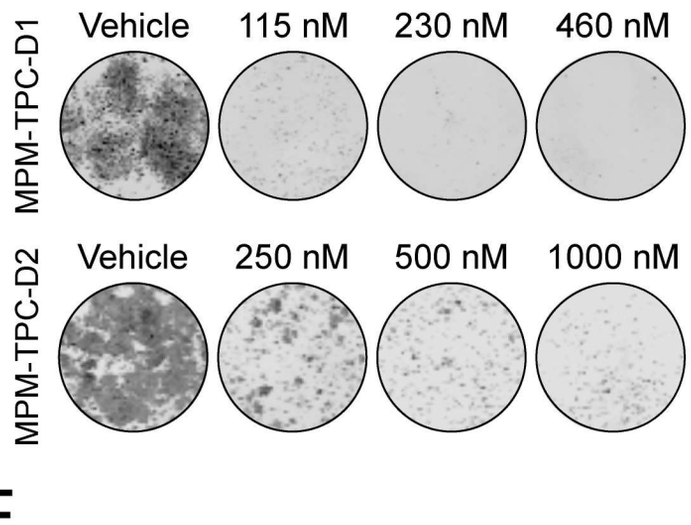
B



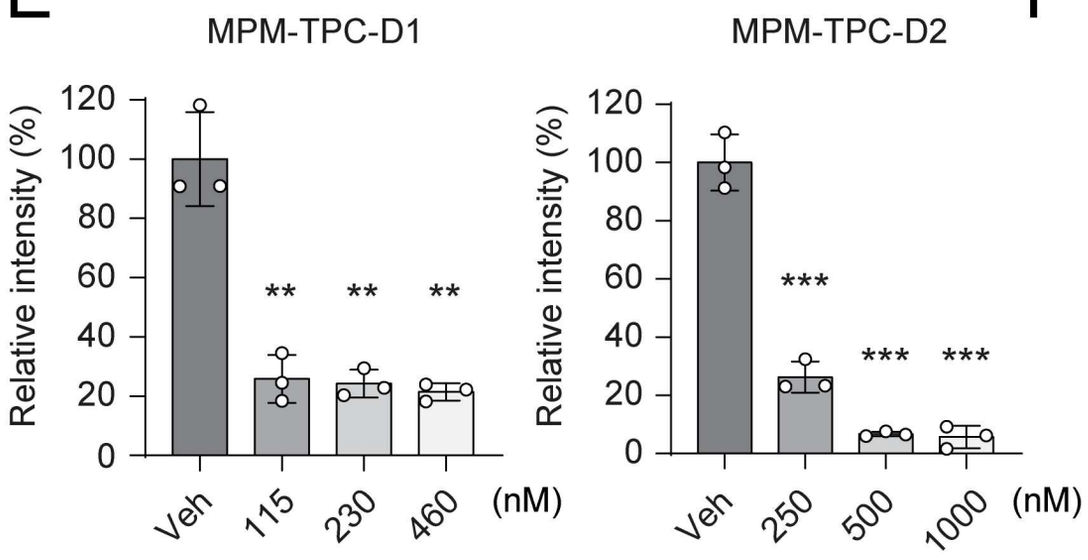
C



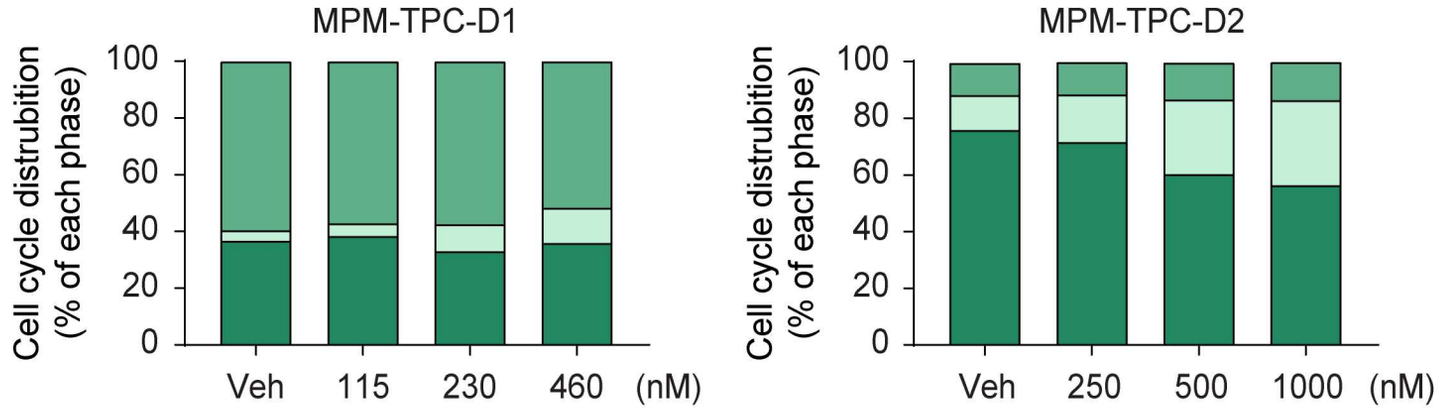
D



E



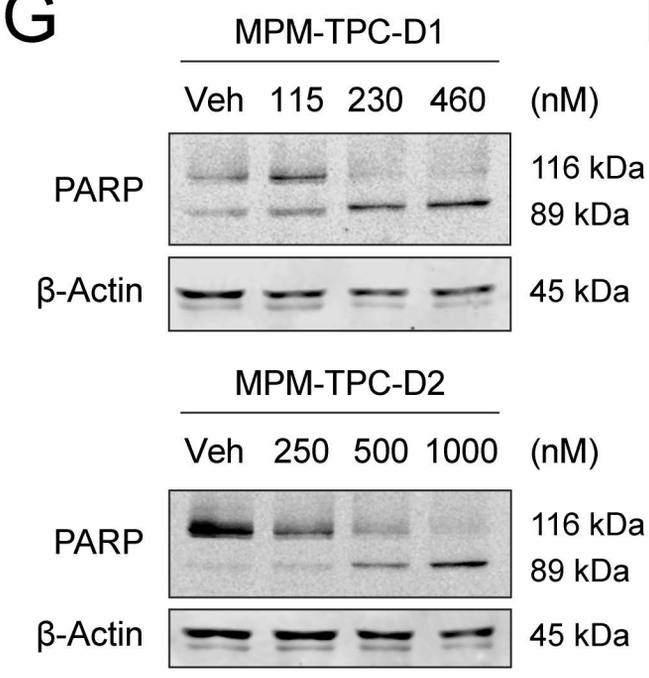
F



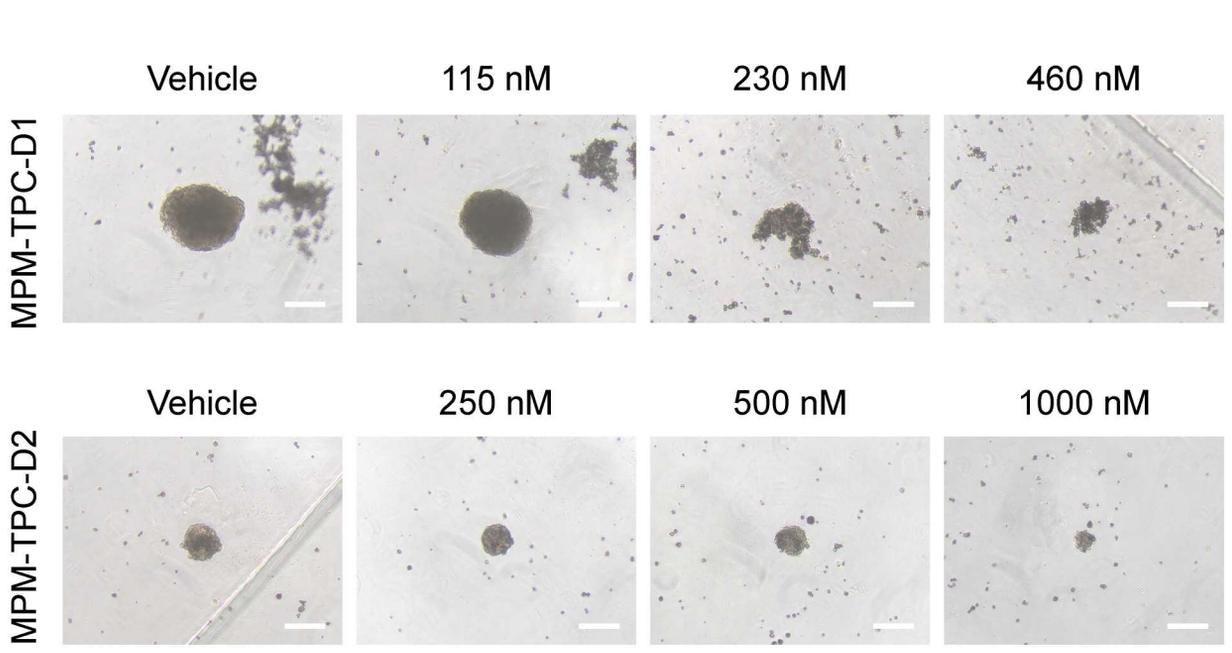
	Vehicle	115 nM	230 nM	460 nM
G1	36.8	38.4	33	36
S	3.19	4.15	9.18	12
G2/M	60	57.4	57.8	52

	Vehicle	250 nM	500 nM	1000 nM
G1	76	71.7	60.4	56.4
S	11.8	16.4	25.9	29.7
G2/M	11.8	11.8	13.4	13.8

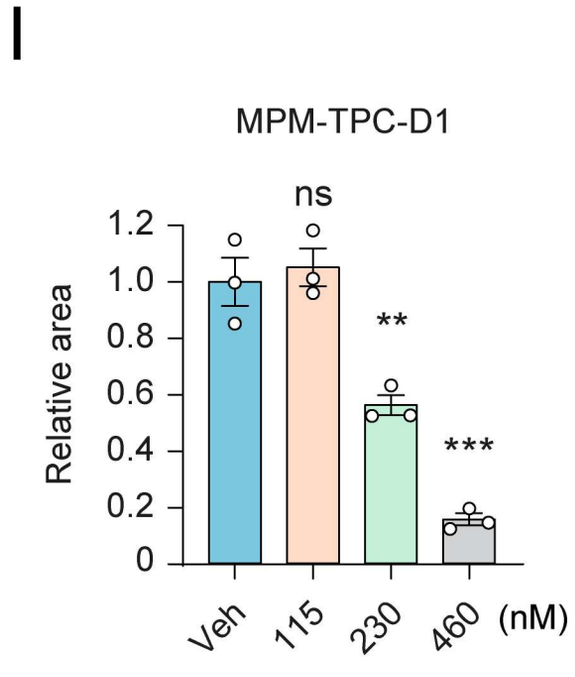
G



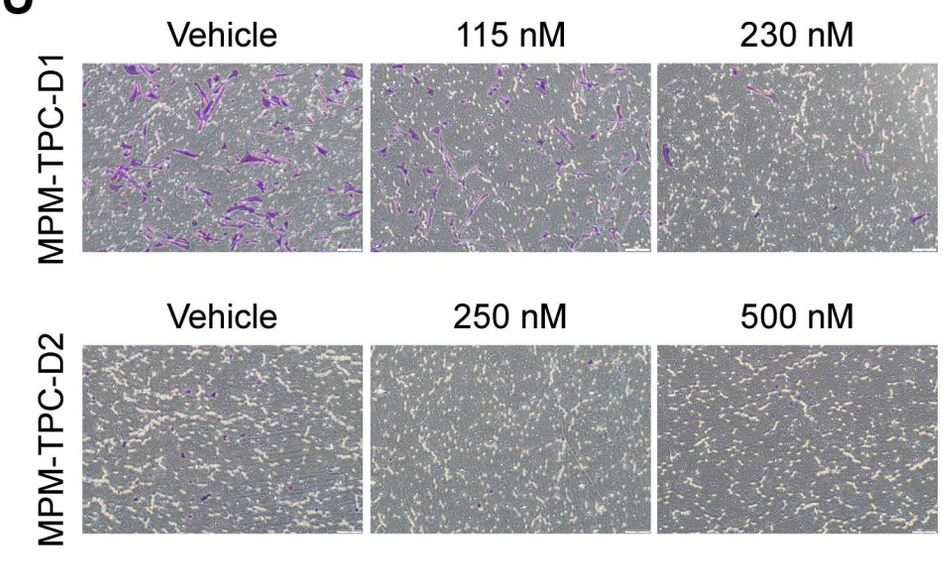
H



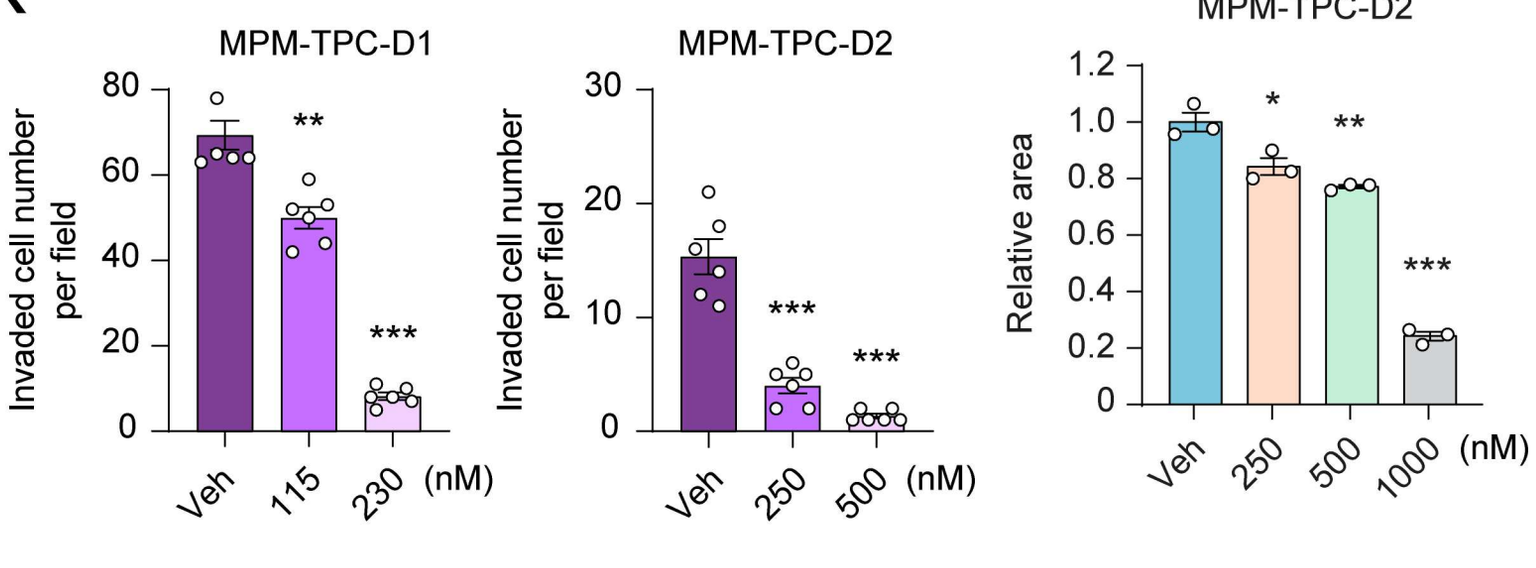
I



J



K



Supplementary Files

This is a list of supplementary files associated with this preprint. Click to download.

- SupplementaryTablesGungorCDDisc04.2026.docx
- SupplementaryGungoretal04.2026.docx